RESEARCH ARTICLE

Scalable Musculoskeletal Model for Dynamic Simulations of Lower Body Movement

Ali Nasr[a] and John McPhee[a]

[a]Department of Systems Design Engineering, University of Waterloo, Canada

ABSTRACT

A musculoskeletal (MSK) model is an important tool for analysing human motions, calculating joint torques during movement, enhancing sports activity, and developing exoskeletons and prostheses. To enable biomechanical investigation of human motion, this work presents an open-source lower body MSK model. The MSK model of the lower body consists of 7 body segments (pelvis, left/right thigh, left/right leg, and left/right foot). The model has 20 degrees of freedom (DoFs) and 28 muscle torque generators (MTGs), which are developed from experimental data. The model can be modified for different anthropometric measurements and subject body characteristics, including sex, age, body mass, height, physical activity, and skin temperature. The model is validated by simulating the torque within the range of motion (ROM) of isolated movements; all simulation findings exhibit a good level of agreement with the literature.

KEYWORDS

Musculoskeletal system model; Dynamic simulation; Biomechanics; Muscle torque; Lower body

1. Introduction

A musculoskeletal model is a useful tool for analyzing complex biomechanical issues [1, 2], simulating and analyzing injuries [3], designing and controlling exoskeletons [4–6], prostheses [7], and rehabilitation robots [8], estimating joint torques in a particular posture or during motion [2], predicting the results of orthopedic procedures [1, 9], optimizing or enhancing movement or tools in sports engineering [10], and researching the central nervous system (CNS) for optimal performance [1, 11–13]. The musculoskeletal system is mechanically complex; thus it is necessary to utilize computer models that are both adequately accurate and relatively efficient [2, 3, 8].

The musculoskeletal system is divided into two subsystems: skeletal and muscular elements [3]. The skeletal system is made up of bones and connective tissues (e.g. ligaments and cartilage). Skeletal muscles are arranged in layers over the bones, and tendons attach them to the bones such that forces produced by the contractile elements of the muscle fibers cause the motions of the body [1].

The majority of musculoskeletal models cannot be easily applied to mechanical tool design challenges that involve human-tool interaction (e.g., golf clubs [10], robotic mechanisms [6], exoskeletons [14], or bicycles [15]) because they are primarily used for biomechanical simulation [3, 9] and not biomechatronics. A more useful model

CONTACT A. Nasr Author. Email: a.nasr@uwaterloo.ca

includes control frameworks for wearable robotic systems [4, 8], biomechanical analysis and synthesis of designed mechanisms [9], and incorporating sensor data (e.g., surface electromyography, electroencephalography, inertial measurement unit, or camera) into control algorithms [4]. Additionally, an musculoskeletal model might be used for real-time data gathering, simulation, and visualization in virtual reality applications with the patient in the simulation loop [16]. One of the objectives of this paper is to develop a user-friendly adjustable model to aid the aforementioned applications.

Biomechanical population-specific models are based on measured data of the population [3, 17]. Therefore, the model should only be used or studied for the specific population [18]. To date, multivariate studies have been conducted to determine the impact of subject variables on peak strength. As a result, regression models for the prediction of strength from anthropometric variables have been proposed [19]. These values, coupled with the properties of the subject body are what the biomechanical model is based on, for example, sex [20], age [20–23], body mass [20, 24, 25], body height [20, 24, 26], dominant side [21, 27], physical activity [28], skin temperature [29–33], impact strength of muscles, anatomical locations, the center of mass (COM), and inertia parameters [34, 35].

In addition, the maximum generated joint moment is limited by the muscle variables (e.g., velocity, and length), tendons, and joint constraints. The nonlinear passive resistive force owing to ligaments and connective tissue around a joint, and muscle activation dynamics are muscular constraints. These biomechanical restrictions may be approximated using either anatomically-detailed muscle tension [36] or muscle torque generators (MTGs) [2, 37]. MTGs enable the reduction of anatomically-detailed muscle complexity models by directly estimating joint constraints [37]. The MTG models have been modified here to take into account anthropometric data and subject body features, similar to [2].

Several commercial (e.g., AnyBody, ADAMS-LifeMOD, MuJoCo, SIMM, SimMechanics, MapleSim) and open-source (e.g., OpenSim, MSMS, RBDL, BiomechZoo) multibody dynamics modelling programs have been used to model and simulate musculoskeletal systems [1]. It is difficult to use the aforementioned software, with the exception of SimMechanics and MapleSim, to augment the human model with sporting equipment, active prostheses, or exoskeleton models [1, 38], particularly when using hydraulic, pneumatic, or flexible components like bike tires [15] or golf shafts [39]. While the other stated programs are focused on numerical calculation, MapleSim is based on symbolic computation and offers analytic derivatives when necessary, such as for optimization or sensitivity assessments.

The distinctive qualities and contributions of this work are, in brief:

A. A flexible, open-source, user-friendly, and simple to add-on (as an external tool) musculoskeletal (MapleSim Biomechanics) model that can extract the lower limb model equations symbolically.
B. A 20-degree of freedom (DoF) lower body skeletal dynamic model that may be adjusted for: (I) sex, (II) body mass, and (III) body height.
C. Modeling of biomechanical joint torques using modified MTGs in accordance with anthropometric values and subject body characteristics, including: (I) sex, (II) age, (III) body mass, (IV) body height, (V) physical activity, and (VI) skin temperature.
D. A generic model for a range of applications, including motion analysis, sports engineering, and the design and control of biomechatronic devices.

This research presents an elucidation of the lower limb model, designed to comple-

ment the existing upper body model introduced in the work by Nasr et al. [2]. This model constitutes an open-source musculoskeletal framework, tailored for the biomechanical analysis of human motion. Notably, this adaptable model can be readily customized to accommodate diverse anthropometric measurements and subject-specific characteristics, encompassing variables such as sex, age, body mass, height, dominant side, physical activity levels, and skin temperature.

In sections 2.1 and 2.2, this study gives the positions and inertia parameters of the lower body model scaled by anthropometric parameters. Second, section 3 introduces the biomechanical joint torque model as a function of biomechanical kinematic factors, anthropometric parameters, and subject body features. The incorporation of a ground reaction model is not within the intended scope of this research. Our primary objective is to offer an evaluation of feasible methodologies in section 4. Following that, the symbolic model extraction is introduced in section 5, two simulation techniques of inverse and forward dynamics are presented in section 6, and the model is validated with the literature data in section 7. An example is given along with a description of the model simulation technique. The discussion of the offered model's applications concludes at section 8.

2. Skeletal dynamic model

2.1. Locations of anatomical landmarks

The global frame is attached to the ground, then, the first segment (the pelvis) has 6-DoF. The torso (a single segment) represents for thorax and abdomen because there does not exist a good estimate for the thoracic joint center [34]. All coordinate frames are defined according to the anatomical landmarks with respect to the International Society of Biomechanics (ISB) standard [40]. Specifically, the joint centres are established in accordance with the literature using the designated anatomical landmarks, and the orientations of the segment coordinate systems are constructed (Figure 1) [34, 40]. The terms and acronyms for the segment anatomical landmarks are taken from [34, 40]. The segment anatomical coordinate systems are established using these important landmarks [34, 35, 40] and presented in Table 1.

The COMs and segment anatomical marker placements for the right body side in Figure 1 are taken from [34]. Following that, the raw location data were scaled to reflect the mean height of each sex (male mean stature 1.77 m, female mean stature 1.61 m), and they are shown in Table 2.

It is assumed that the right and left limbs are symmetrical. Similar to [2], the matrix in Equation (1) transforms the position of anatomical landmarks and segment COMs from the right limb (presented in Table 2) to the left limb.

$$R_{R2L} = \begin{bmatrix} 1 & 0 & 0 \\ 0 & 1 & 0 \\ 0 & 0 & -1 \end{bmatrix} \tag{1}$$

2.2. Body segment inertia parameters

It is common practise to calculate body segment inertial parameterss using published linear or non-linear regression formulae [34, 35, 41, 42]. In Table 3, the mass of each

Table 1.: Abbreviations and descriptions for anatomical coordinate systems used in the lower body kinematic model according to ISB standard [34, 35, 40].

Segment	Origin /Axis	Description (refer to Figure 1)
Thigh	O	Coincidence with the HJC
	Y	The line connecting the KJC to the HJC, pointing superiorly
	X	The line prependicular to the plane containing the HJC, LFE and MFE, pointing anteriorly
	Z	The cross product of the X- and Y-axes
Leg	O	Coincidence with the KJC or the midpoint between the LFE and MFE
	Y	The line connecting the LJC to the KJC, pointing superiorly
	X	The line prependicular to the plane containing the KJC, the AJC and the Fibula Head (FH), pointing anteriorly
	Z	The cross product of the X- and Y-axes
Foot	O	Coincidence with the AJC or the midpoint between the LM and SPH
	X	The line connecting the Calcaneous (CAL) to the midpoint between the 1st and 5th Metatarsal Heads (MHI and MHV), pointing anteriorly
	Y	The line prependicular to the plane containing the CAL, MHI and MHV, pointing superiorly
	Z	The cross product of the X- and Y-axes

Table 2.: Scaled 3D placements of anatomical landmarks and the segment COMs relation to the segment anatomical coordinate systems for both sex (right limb) [34, 35].

Segment	Reference Coordinate System	Anatomical Landmark (refer to Figure 1)	Scaled 3D position to height (%)					
			Female			Male		
			X	Y	Z	X	Y	Z
Pelvis	LJC	HJC (Hip Joint Center)	3.35	-5.78	5.47	3.16	-4.24	4.58
		COM	-0.06	-1.55	0.00	0.17	-1.47	0.00
Thigh	HJC	LFE (Lateral Femoral Epicondyle)	0.00	-23.29	3.54	0.00	-24.35	3.22
		MFE (Medial Femoral Epicondyle)	0.00	-23.73	-3.54	0.00	-24.41	-3.22
		KJC (Knee Joint Center)	0.00	-23.51	0.00	0.00	-24.38	0.00
		COM	-1.80	-8.88	0.19	-1.02	-10.45	0.79
Leg	KJC	FH (Fibula Head)	0.00	-2.48	3.73	0.00	-1.30	2.66
		SPH (Sphyrion)	0.62	-24.04	-1.93	1.19	-24.52	-1.86
		LM (Lateral Malleolus)	-0.62	-24.22	1.93	-1.19	-24.46	1.86
		AJC (Ankle Joint Center)	0.00	-24.13	0.00	0.00	-24.49	0.00
		COM	-1.18	-9.75	0.75	-1.19	-10.06	0.17
Foot	AJC	CAL (Calcaneous)	-3.66	-2.86	0.75	-2.60	-1.19	0.40
		MHI (1st Metatarsal Head)	7.20	-2.86	-2.05	8.25	-1.19	-2.66
		MHV (5th Metatarsal Head)	6.02	-2.86	3.54	7.23	-1.19	2.66
		TTII (2nd Toe Tip)	10.81	-3.35	0.56	12.37	-2.77	0.51
		COM	2.80	-2.24	0.37	2.54	-2.03	0.34

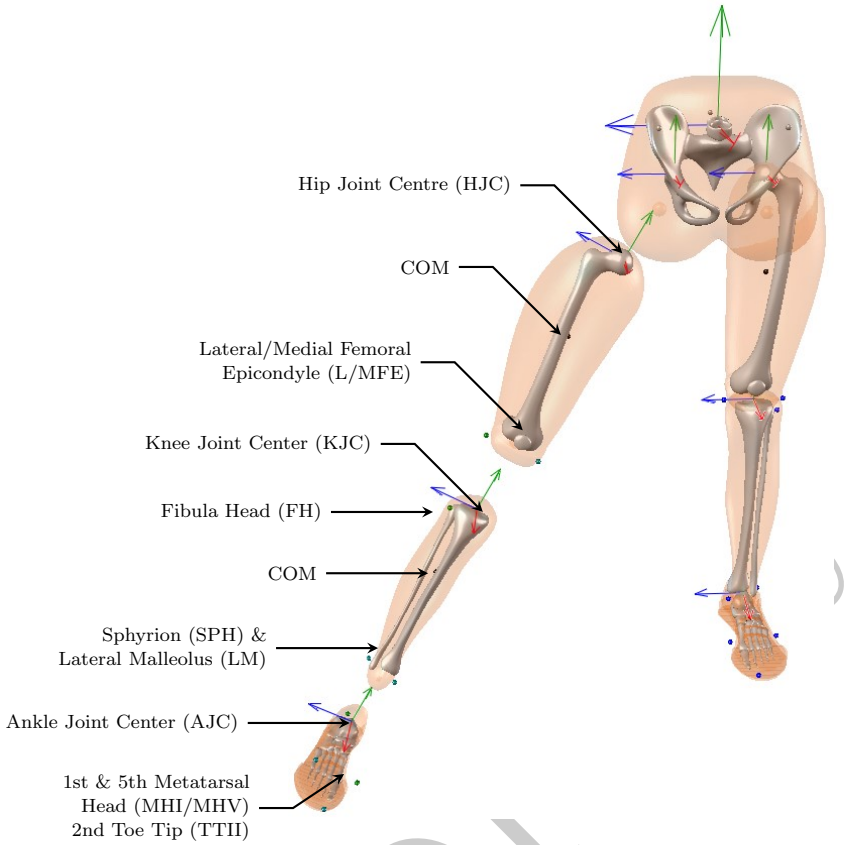

Figure 1.: Locations of specific anatomical landmarks of lower limb and the resulting segment coordinate system orientations in accordance with ISB standard [34, 40].

segment (M) is shown as a proportion of the body's overall mass [35]. The inertia tensor is determined according to the origin of segment coordinate axes. Specifically, similar to [2], Equation (2) expresses the segment inertia matrix (I) in relation to the segment length (L) and the segment mass (M) for the right limb. In Table 3, scaling factors (r_{ij}) for the inertia matrix are shown together with scaled segment lengths (L) to body height and (M) to body mass.

$$I_R = ML^2 \begin{bmatrix} r_{xx}^2 & r_{xy}^2 & r_{xz}^2 \\ r_{xy}^2 & r_{yy}^2 & r_{yz}^2 \\ r_{xz}^2 & r_{yz}^2 & r_{zz}^2 \end{bmatrix} \tag{2}$$

By converting the equivalent right limb inertia matrix of Equation (2) by Equation (3), which uses the matrix of Equation (1), it is possible to determine the segment inertia matrix of the left lower limb.

$$I_L = R_{R2L}^T I_R R_{R2L} \tag{3}$$

Table 3.: The inertia tensor's female and male segment scaling masses, lengths, and scaling factors [34, 35]. The unit imaginary number is i.

Segment	Origin	Length definition	Scaled mass (%)		Scaled length (%)		Scaling factors for the inertia tensor $[r_{xx}, r_{yy}, r_{zz}, r_{xy}, r_{xz}, r_{yz}](\%)$	
			Female	Male	Female	Male	Female	Male
Pelvis	LJC	LJC to HJC	14.60	14.20	6.65	5.31	$[91, 100, 79, 34i, i, i]$	$[101, 106, 95, 25i, 12i, 8i]$
Thigh	HJC	HJC to KJC	14.60	12.30	23.54	24.41	$[31, 19, 32, 7, 2i, 7i]$	$[29, 15, 30, 7, 2i, 7i]$
Leg	KJC	KJC to AJC	4.50	4.80	24.10	24.46	$[28, 10, 28, 2, 1, 6]$	$[28, 10, 28, 4i, 2i, 5]$
Foot	AJC	AJC to TTII	1.00	1.20	10.25	10.34	$[17, 36, 35, 10i, 6, 4i]$	$[17, 37, 36, 13, 8i, 0]$

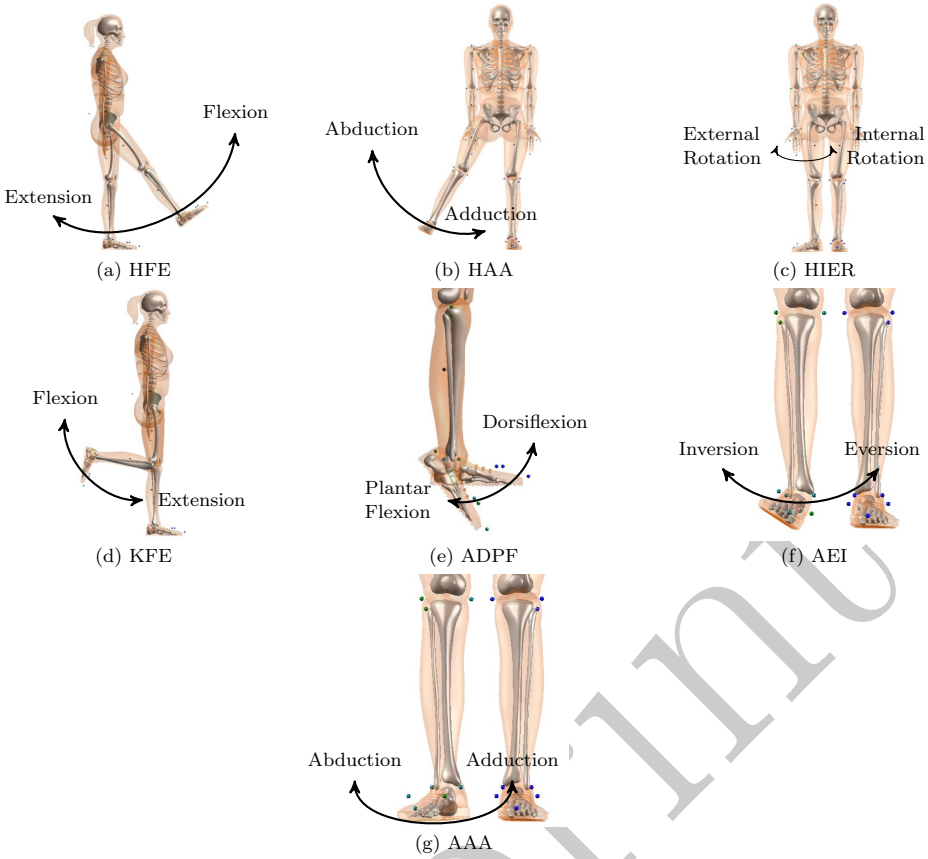

Figure 2.: Depiction of lower body musculoskeletal model DoF and directions for (a) HFE, (b) HAA, (c) HIER, (d) KFE, (e) ADPF, (f) AEI, (g) AAA.

2.3. Degrees of freedom

The provided lower body kinematic model has 20 DoF: 6 DoF for pose (position and orientation) of the pelvis in 3D space, 3 DoF for each hip (hip flexion/extension (HFE), hip adduction/abduction (HAA), and hip internal/external rotation (HIER)), 1 DoF for each knee (knee flexion/extension (KFE)), and 3 DoF for each ankle (ankle dorsiflexion/plantar flexion (ADPF), ankle eversion/inversion (AEI), and ankle adduction/abduction (AAA)). The definitions and motion of DoF in the lower body kinematic model are shown in Table 4 (visualized in Figure 2). The left lower limb has reversed directions for HAA, HIER, AEI, and AAA compared to Table 4 (right lower limb information).

3. Biomechanical joint torque model

The amount of torque that can be created around each joint by human muscles is influenced by a number of phenomena. The following is a list of the important variables that influence muscle force: the muscle velocity, the muscle length, the muscle excitation delay, and nonlinear passive force generation due to ligaments and connective tissues surrounding the joint.

Muscle modelling often use a 3-element Hill-type muscle-tendon unit (Figure 3a)

Table 4.: DoF abbreviations and meanings, the mean range of motion (ROM) for female and male, the average maximum angular velocity of the lower-body joints, and the polynomial coefficients of torque-angle scaling functions (normalized isometric torque functions).

Joint	DoF	Axis	Direction	θ_{max} (rad)			$\lvert\omega_{max}\rvert$ (rad/s)		Polynomial Coefficient of Torque-angle Scaling Function in Equation (7)			
				Female	Male	Ref	Mean	Ref	p_1	p_2	p_3	Ref
Pelvis	X	X-axis	+ North - South									
	Y	Y-axis	+ Up - Down									
	Z	Z-axis	+ West - East									
	X	X-axis	+ Right roll - Left roll									
	Y	Y-axis	+ Right yaw - Left yaw									
	Z	Z-axis	+ Right pitch - Left pitch									
Hip	HFE	Z-axis	+ Flexion	2.276	2.211	[43]	12.00	[44]	1	-0.0044	-0.1492	[45]
			- Extension	-0.281	-0.312	[43]	14.10	[44]	0.4187	0.7945	-0.2715	[45]
	HAA	X-axis	+ Adduction	0.243	0.239	[43]	2.41	[46]	0.9961	-0.2027	-2.6258	[47]
			- Abduction	-0.595	-0.560	[43]	3.14	[46]	0.8497	-1.5285	-3.8854	[47]
	HIER	Y-axis	+ Internal Rotation	0.836	0.648	[43]	4.22	[48]	0.9997	0.0392	-1.132	[49]
			- External Rotation	-0.709	-0.815	[43]	6.12	[48]	0.9998	-0.0378	-1.34	[49]
Knee	KFE	Z-axis	+ Extension	0.093	0.035	[43]	28.40	[44]	0.3385	-1.066	-0.4294	[45]
			- Flexion	-2.599	-2.567	[43]	18.60	[44]	0.5369	-0.8421	-0.3828	[45]
Ankle	ADPF	Z-axis	+ Dorsiflexion	0.417	0.389	[43]	12.70	[44]	0.9403	-0.535	-1.1989	[50]
			- Plantar Flexion	-0.944	-0.874	[43]	12.60	[44]	0.955	-0.5544	-1.7042	[50]
	AEI	X-axis	+ Eversion	0.300	0.227	[51]	2.64	[52]	0.7639	0.6787	0.3589	[50]
			- Inversion	-0.374	-0.342	[51]	6.75	[52]	0.9005	-0.6333	-1.0073	[50]
	AAA	Y-axis	+ Adduction	0.625	0.578	[51]	4.22	[48]	0.6843	-0.5254	-0.1076	[53]
			- Abduction	-0.702	-0.630	[51]	4.50	[48]	0.8808	0.315	-0.1982	[53]

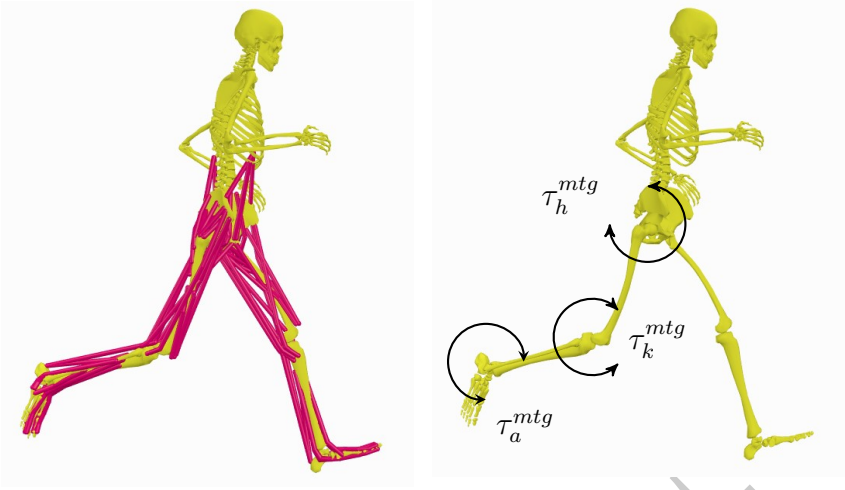

(a) Anatomically detailed muscles (b) Muscle torque generators

Figure 3.: Schematic of the hip, knee, and ankle joint, actuated by (a) Hill-type muscles and (b) MTGs. Note the complex muscle route geometry and redundancy encountered when using detailed muscle models.

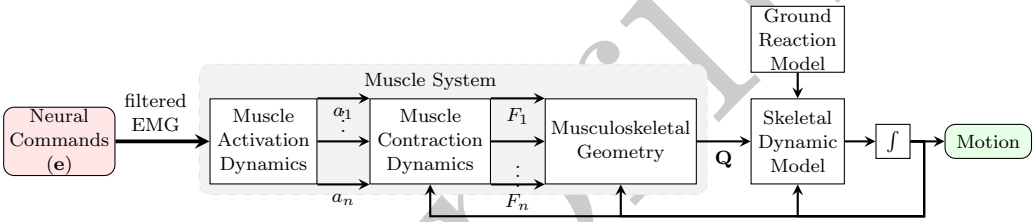

Figure 4.: Forward simulation of a multi-muscle musculoskeletal system. a_i and F_i stand for the activation signal and the muscle force, respectively [2].

[36]. To approximate the muscle-tendon geometry, moving and wrapping points are also utilised [36]. Each muscle model in Figure 4 consists of two components: an active contractile piece (which generates active force) and a passive parallel-elastic element (with viscoelasticity). The model is completed with a nonlinear series-elastic component that describes the mechanical properties of the tendon. It is challenging to obtain parameters for complicated muscle models of this kind. Additionally, because in vivo human studies are required for the parameter identification (for example, muscle force cannot be measured directly), they cannot be empirically tested.

As asserted by Yeadon et al. [54] and Inkol and McPhee [55], muscle fiber lengths exhibit a direct correlation with joint angles. Additionally, muscle fiber velocities are intrinsically linked to joint angular velocities. Both of these factors exert a notable influence on muscle forces. Furthermore, the transformation of muscle forces into joint torque necessitates intricate geometric modeling of muscle attachments to the skeletal structure. Without the requirement to represent muscle geometries and forces, an MTG model provides a joint torque that mimics the biomechanics of muscles and joint limitations (Figure 3b) [37]. Specifically, the torque-angle (τ_θ) and torque-speed (τ_ω) relationships, as seen in Figure 5, are two explicit examples of how the MTG model mimics muscle force generation. In torque-driven simulation, the MTG models

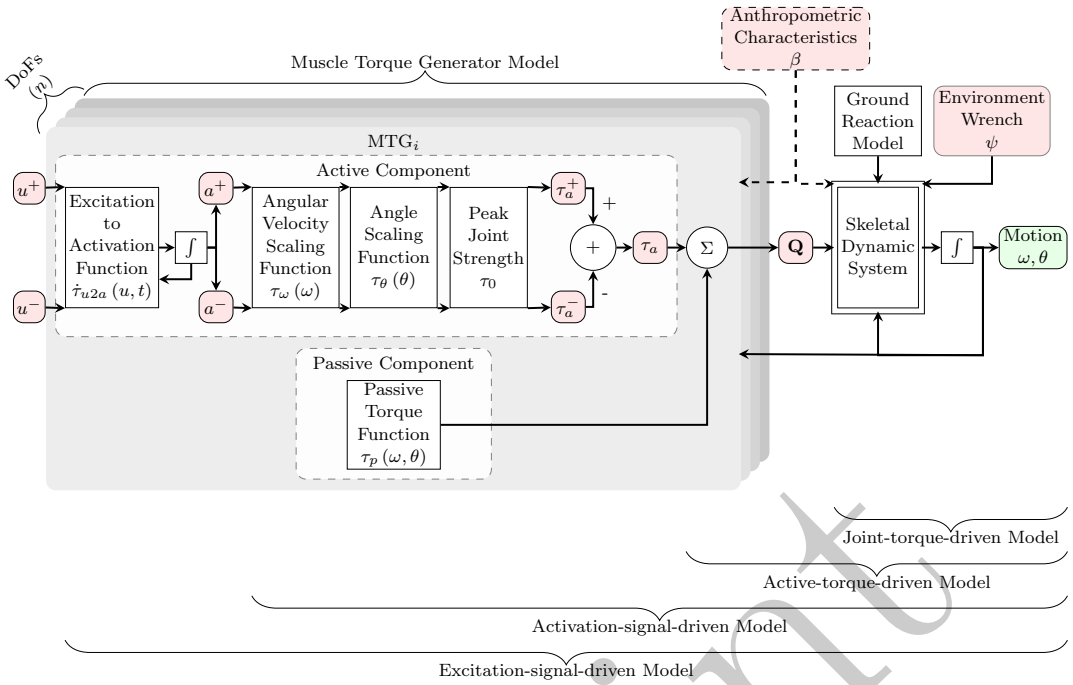

Figure 5.: Diagrams of forward simulation of a musculoskeletal system using MTGs. Two active components for two excitation signals (positive and negative directions) and one passive component make up the MTG model [2].

provide torque at each joint based on the kinematics of that joint (monoarticular assumption) [56].

Every MTG model has a distinct set of properties, including an active component (creates the active torque as a function of the joint's angle and angular velocity) and a passive component (mimicking the joint's minimal viscosity or friction and limiting the joint ROM). The human joint torque (τ_h) as determined by the MTG model is illustrated in Equation (4) [10, 37].

$$\tau_h(t) = a^+\left(u^+, t\right)\tau_\omega^+(\omega)\,\tau_\theta^+(\theta)\,\tau_0^+ + a^-\left(u^-, t\right)\tau_\omega^-(\omega)\,\tau_\theta^-(\theta)\,\tau_0^- + \tau_p(\theta,\omega) \tag{4}$$

where

- $a(u,t)$ the activation signal (computed from excitation-to-activation ordinary differential equation function), which is illustrated in section 3.5 and Equation (9)
- $\tau_\omega(\omega)$ the active-torque-angular-speed-scaling function, which is illustrated in section 3.4 and Equation (8)
- $\tau_\theta(\theta)$ the active-torque-position-scaling function, which is illustrated in section 3.3 and Equation (7)
- $\tau_p(\theta,\omega)$ the passive torque function due to viscous damping and nonlinear stiffness, which is illustrated in section 3.1 and Equation (5)
- τ_0 the peak isometric joint torque-producing capability

The net active joint torque, which the biomechanical model produces, is

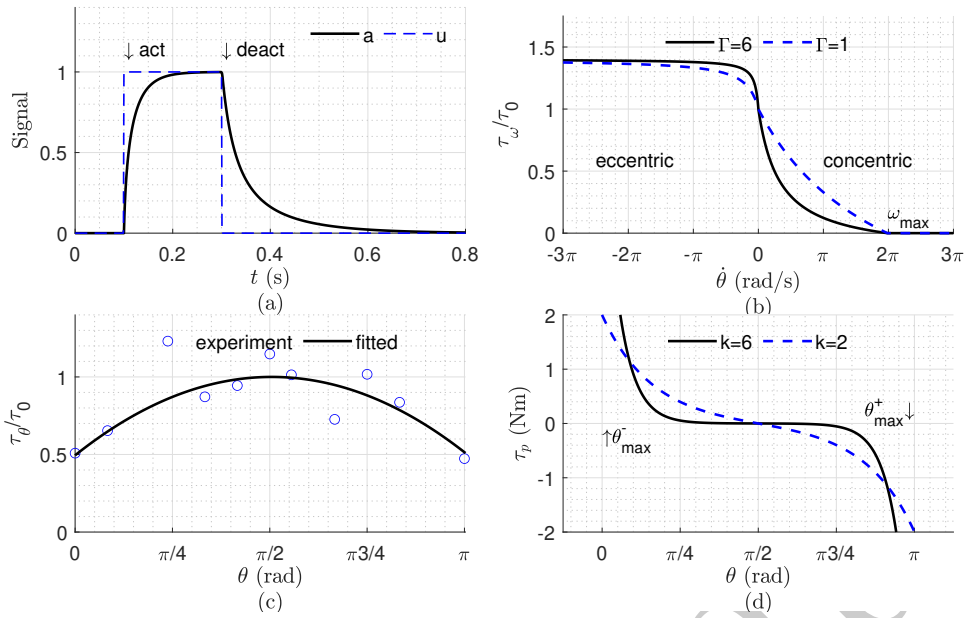

Figure 6.: Examples of MTG curves that represent tendon and muscle forces: excitation-to-activation signal conversion (a), the active-torque-angular-speed scaling curve (b), the active-torque-angle scaling curve (c), and the passive torque curve (d) [2].

$a(u,t)\,\tau_\omega(\omega)\,\tau_\theta(\theta)\,\tau_0$. The activation signal $a(t)$ or the excitation signal $u(t)$, which can have a value between 0 and 1 serves as the control input to the MTG model. The examples of these four functions are depicted in Figure 6.

Each DoF (joint axis of rotation) was controlled by two active components of MTGs (28 total products of $a(u,t)\,\tau_\omega(\omega)\,\tau_\theta(\theta)\,\tau_0$): one for each of the two directions (negative and positive) of joint rotation (two for each joint). Moreover, for each DoF (joint axis of rotation), one passive component of MTG (20 total $\tau_p(\theta,\omega)$)) was employed. As a result, the musculoskeletal system is over-actuated and needs to resolve actuation redundancy, potentially with an optimization solution. Each active MTG component was only allowed to operate within a maximum torque range of τ_0^+ for positive MTGs and τ_0^- for negative MTGs.

By fitting the functions to experimental data, one may determine the parameters of Equations (4-8). To collect experimental data, a computerised robotic dynamometer is often used in orthopaedic and sports medicine applications. The human dynamometer is a tool used to gauge the net torque produced by a single isolated joint. Both isometric (constant muscle length) and isokinetic (constant speed) joint conditions are suitable for its application.

3.1. Passive torque function

When the surrounding muscles, tendons, and ligaments are stressed, passive torques develop [57]. Moreover, close to anatomical joint limitations, passive joint torques increase significantly [57–59] (exemplified in Figure 6d). Usually, to mimic the viscous damping and nonlinear stiffness of the joint a double exponential function is used, similar to Equation (5) [60]. Accordingly, this function restricts the joint's location

inside its ROM [60]. Specifically, a large restoring torque results from θ exceeding the boundaries of the ROM (specified by breakpoints of θ^{-}_{max} and θ^{+}_{max}). Equation (5) also includes the damping element to reflect viscoelasticity.

$$\tau_p\left(\theta,\omega\right) = k_1 e^{-k_2(\theta-\theta^{-}_{max})} - k_3 e^{k_4(\theta-\theta^{+}_{max})} - c\ \omega \tag{5}$$

where

θ	the joint angle
k	the passive parameters identified from analysing experimental data and fitting the nonlinear function
θ^{-}_{max}	the maximum ROM for negative direction, which is illustrated in Table 4
θ^{+}_{max}	the maximum ROM for positive direction, which is illustrated in Table 4
c	the linear coefficient of rotational damping

The nonlinear function is often fitted to experimental data to get the passive parameters (k_i), which range from 0.5 to 6 [10]. Based on our experimental findings, k_i should be less for the weaker joints such as HIER, AEI, and AAA. It is advised that the linear damping coefficient (c) be about 0.1 Nm/rad [60] for most joints.

θ_{max} for the HAA, HIER, AEI, and AAA of the left limb is the negative of the value in Table 4 (which is for right limb).

3.2. Peak joint strength

The average peak isokinetic torque for non-athletic females and males, together with the corresponding anthropometric measurements are provided in Table 5. Based on the variables in Table 5, the mean maximum isometric joint torque for each non-athletic adult male or female is estimated. Based on the anthropometric characteristics presented in Table 5 the intercept (β_1) and sex (β_2) parameters were extrapolated. Equation (6) reflects the regression of the mean peak isometric torque.

$$\begin{aligned}\tau_0 = \ & \left(\beta_1 + \beta_2\ s + \beta_3\ a + \beta_4\ h + \beta_5\ m\right)\ \left(1 - \tfrac{\mu}{2} + \mu\ d\right)\ \left(1 + \varsigma\ w\right) \\ & \left[1 + \rho\ \left(10 + \tfrac{20\arctan\left[(T-30)\pi/20\right]}{\pi}\right)\right]\end{aligned} \tag{6}$$

where

β_i	the anthropometric and torque measurements shown in Table 5
s	the subject's sex constant (for a male is 1 and for a female is 0)
a	the subject's age in year
h	the subject's height in meter
m	the subject's body mass in kilogram
w	the subject's physical activity in number of workout sessions per week
d	the subject's dominant side constant (for a dominant side is 1 and for a non-dominant side is 0)
T	the subject's skin temperature in Celsius
μ	the maximum strength difference between dominant and non-dominant sides
ς	the impact of exercise on maximum muscular strength

ρ	the impact of skin temperature (0.03 for each degree between 20^o to 40^o) (unit-less)

The joint torque is shown for the average of both sides in Table 5. Particularly, the dominant side can offer a mean value of 9% greater strength than the non-dominant side [61, 62]. As a result, 0.09 is chosen as the side parameter (μ) for the lower limb. The joint torque for healthy non-athletic participants (w=0) is shown in Table 5. A mean value supplied by [63] for training time per week is represented by ς and is equal to 0.065. According to Ekblom and Bergh [32], the peak muscle torque increases 3% for each skin temperature more than 20^o, no more than 40^o. We used arctan instead of simple slope to limit the maximum of impact of skin temperature.

3.3. Active-torque-angle scaling function

The joint isometric torque is inconsistent across the whole ROM due to the non-linear tendon force-length relation (exemplified in Figure 6c). The active-torque-angle curve is generally represented in the literature using second-order or fourth-order polynomial functions [54, 72–74] using the summation notation in Equation (7).

$$\tau_\theta(\theta) = ramp\left(\sum_{k=1}^{n+1} p_k \theta^{k-1}\right) \tag{7}$$

where

θ	the joint angle
p_k	the coefficient of the polynomial, which is provided in Table 4
n	the order of polynomial functions

and $\tau_\theta(\theta)$ is normalized by the peak isometric torque of each joint. As a result, the value of $\tau_\theta(\theta)$ at the optimum angle is 1.

The maximal isometric torque should be accessible for every ROM in order to fit the polynomial functions to the experimental data. Due to a lack of available data for all ROMs, the fitted polynomial function may be zero or even negative for ranges outside of the specified angle ROMs. One solution is that the edge torque, which is estimated or assumed joint torque at the maximum ROM, is assumed as the average of fitted polynomial and interpolation with nearest joint torque.

The left limb has reverse positive and negative directions for HAA, HIER, AEI, and AAA. In Table 4, the even index of p_k for the HAA, HIER, AEI, and AAA DoF of the left lower limb has a reversed sign.

3.4. Active-torque-angular-speed scaling function

Muscular velocity affects muscular strength. Consequently, the joint angular velocity (ω) scales the active torque (τ_a) (active-torque–angular-speed correlation, exemplified in Figure 6b). According to [75–78] and adopted from a linearized Hill model structure, a rational piecewise instantaneous isokinetic torque function of joint angular velocity

Table 5.: Peak joint torque for non-athletic females and males (mean of dominant and non-dominant limb) and calculated parameters of peak isokinetic torque for non-athletic participants with the anthropometric variables of body age, height, mass, and sex.

Joint	DoF	Direction	Female						Male						β_1 (Nm)	β_2 (Nm)	β_3 (Nm/year)			β_4 (N)			β_5 (Nm/kg)		
			Torque (Nm)	Age (year)	Height (m)	Mass (kg)	Population	Ref	Torque (Nm)	Age (year)	Height (m)	Mass (kg)	Population	Ref			Mean	Range	Ref	Mean	Range	Ref	Mean	Range	Ref
Hip	HFE	+	126.1	22.2	1.70	67.3	10	[45]	148.5	26.2	1.79	85.1	10	[64]	-121.16	0.68	-0.92	-1.50 : -0.35	[20]	125	-91 : 298	[20]	0.82	-0.20 : 2.06	[20]
		-	205.4	22.2	1.70	67.3	10	[45]	182.4	26.2	1.79	85.1	10	[64]	-41.86	-44.68									
	HAA	+	131.6	20.1	1.61	57.2	44	[65]	202.5	25.5	1.80	75.0	80	[65]	-98.60	37.94									
		-	137.3	20.1	1.61	57.2	44	[65]	202.5	25.5	1.80	75.0	80	[65]	-92.88	32.22									
	HIER	+	32.1	24.4	1.70	68.4	15	[66]	37.4	25.8	1.79	81.3	15	[66]	-213.74	-15.42									
		-	25.3	24.4	1.70	68.4	15	[66]	45.5	25.8	1.79	81.3	15	[66]	-220.58	-0.44									
Knee	KFE	+	182.8	22.2	1.70	67.3	10	[45]	235.9	19.1	1.78	71.5	438	[67]	-12.13	37.84	-1.22	-1.88 :-0.73	[20]	89	-112 :200	[20]	1.05	0.12 :1.98	[20]
		-	104.1	22.2	1.70	67.3	10	[45]	158.5	19.1	1.78	71.5	438	[67]	-90.78	39.09									
Ankle	ADPF	+	33.0	22.2	1.70	67.3	10	[45]	36.2	19.1	1.78	71.5	438	[67]	-24.57	-0.21	-0.04	-0.17 : 0.05	[20]	14	-111 : 119	[20]	0.515	-0.05 : 1.08	[20]
		-	108.6	22.2	1.70	67.3	10	[45]	130.0	19.1	1.78	71.5	438	[67]	51.03	17.99									
	AEI	+	19.5	23.3	1.65	57.1	20	[68]	13.0	22.6	1.80	77.2	20	[69]	-32.07	-18.95									
		-	26.4	23.3	1.65	57.1	20	[68]	31.2	22.6	1.80	77.2	20	[69]	-25.17	-7.65									
	AAA	+	17.0	16.9	1.57	49.9	81	[70]	40.5	22.1	1.85	82.9	22	[71]	-30.04	2.83									
		-	14.0	16.9	1.57	49.9	81	[70]	34.9	22.1	1.85	82.9	22	[71]	-33.03	0.22									

is implemented:

$$\tau_{\omega}(\omega) = \begin{cases} 0 & \omega \geq \omega_{max} \\ \frac{|\omega_{max}|-\omega}{|\omega_{max}|+\Gamma\omega} & \omega_{max} < \omega < 0 \\ 1 & \omega = 0 \\ \frac{(1-R)|\omega_{max}|+S\omega R(\Gamma+1)}{(1-R)|\omega_{max}|+S\omega(\Gamma+1)} & \omega < 0 \end{cases} \tag{8}$$

where

ω	the joint's instantaneous angular velocity
$\lvert\omega_{max}\rvert$	the absolute value of the joint's maximum angular velocity that results in no torque generation, as shown in Table 4
Γ	the shape factor affecting the curvature of the torque-velocity hyperbola concentric relationship
S	the slope of eccentric to concentric phase transition (at zero angular velocity) defined by [77]
R	the maximum eccentric isokinetic torque (τ_0) divided by maximum isometric torque (τ_0)

In Equation (8), for the $\omega \geq 0$ condition, $\tau_{\omega}(\omega)$ has a potential singularity as ω proceeds toward $-|\omega_{max}|/\Gamma$ instantaneous angular velocity. Consequently, the force-velocity scaling relationship differs from Hill-type's model [36] when the force is greater than the isometric tension (τ_0); it also has different output when $\omega < 0$ [77, 79]. As a result of $\tau_{\omega}(\omega)$ normalization by the maximal isometric torque of each joint, the value of $\tau_{\omega}(\omega)$ is 1 at zero velocity.

Γ is valued around 3, according to [39]. the value for S ranges from roughly 2 [10, 77] to 3 [80]. Additionally, the value of R ranges from 1.4 [76] to 1.5 [77]. Equation (8) utilised a negative ω to represent motions in negative directions.

3.5. Excitation-to-activation signal function

Excitation-to-activation signal function, sometimes referred to as activation dynamics, serves as a representation of the muscle fibre recruitment state [81]. The period between receiving a signal (neural excitation) and turning it into action potentials to activate muscle fibres via electrochemical processes in the muscle tissue is delayed by the activation dynamics [81] (exemplified in Figure 6a). Data from trials' post-processed electromyography can be utilised to create a collection of activations [82].

According to this, an excitation-to-activation function is used for muscle groups near joints to imitate the activation signal produced by a brain drive (regardless of joint angle) [80]. Theoretically, when the torque generator engages and disengages, the activation signal function combines the period at which the muscles are active and inactive, respectively. Logically speaking, the time lag brought on by the electrochemical activity produced by the action potential that causes muscle contraction is equivalent to the excitation-to-activation signal function. Equation (9), which was adapted from the Hill-type muscle model, is a modified function for an excitation-to-activation signal [83]. A nonlinear function and a linear first-order differential equation make up

the excitation-to-activation dynamic model [84, 85]. The CNS's excitation signal $u(t)$ is transformed into the activation signal $a(t)$, which represents the level of muscle activation, via the first-order differential equation.

$$\dot{a} = \begin{cases} \frac{u-a}{t_{act}(0.5+1.5a)} & u \geq a \\ \frac{(u-a)(0.5+1.5a)}{t_{deact}} & u \leq a \end{cases} \tag{9}$$

where

u	the excitation signal
a	the activation signal
t_{act}	the muscle activation time constants
t_{deact}	the muscle deactivation time constants

In the case of an adult subject, t_{act} may have a value of $40+0.25\times$age ms, according to [86], and t_{deact} is taken to be equal to $4t_{act}$. For monoarticular muscles, the excitation signal falls within the range of $[0, 1]$.

4. Ground reaction model

The inclusion of a ground reaction model falls beyond the scope of this study; our focus here lies in providing a review of potential methodologies in this regard. Contact models used in multibody human models are explored, with a primary focus on foot-ground contact, crucial for simulating walking, running, and jumping. Other contacts of interest include posterior-seat contact [87], crutch-ground contact [88], and exoskeletons [6, 13, 89].

4.1. Normal force models

The normal force models are categorized based on complexity, starting with rigid joint representations suitable for continuous contact, like foot-ground contact during squatting [90]. For intermittent contact, kinematic constraints and reaction forces are applied during contact phases. Rigid contact models in 2D use two point constraints for each foot [91, 92], while 3D models may use one [93] to six [94] point constraints per foot, depending on the foot model.

Deformable contact models are introduced in [1], with point-contact models being the simplest, using linear or non-linear springs and dampers at one point on the contact surface. To accurately model foot-ground contact, one can utilize multiple point contacts distributed across the surface. Another approach involves a single point of contact that moves relative to the foot, which is based on a geometrical representation of the contact surface using models such as spheres, superellipsoids, or disk-plane configurations [95]. Volumetric contact models, which utilize elastic foundation theory to represent contact loads distributed across a surface, have also been investigated [96]. Foot-ground contact has been studied using finite element contact models; however, these models are computationally demanding in comparison to alternative approaches [97].

4.2. Friction force models

Friction may be modeled using penalty functions to limit friction forces [91]. For deformable contacts, velocity-based friction models approximate Coulomb friction using non-linear functions of velocity [96, 98, 99]. However, they may not accurately represent low-velocity scenarios, common in human motion. Position-based friction models, like bristle friction models, use tangential springs and are more accurate in cases of stick-and-slip behavior [100]. Existing models have not thoroughly explored the lateral flexibility of the contact surface, which is influenced by soft tissues in the human body. This aspect could be effectively addressed by incorporating position-based friction models. Another potential model is the Maw friction model [101], suitable for modeling stick and slip conditions in different regions of the contact surface, applicable to biomechanical models like foot contact during gait.

5. General structure of dynamic equations

The dynamic musculoskeletal model can be exported in one of four ways, as illustrated in Figure 5: (I) joint-torque-driven, (II) active-torque-driven, (III) activation-signal-driven, and (IV) excitation-signal-driven. Only the dynamic model of the skeletal system is present at the joint torque-driven level. The skeletal system and the passive torque function are the two components of the active-torque-driven level. The dynamic model of the skeletal system and the MTG model without the excitation-to-activation dynamic model make up the activation-driven level. The skeletal system and the whole MTG model with the excitations as input make up the fourth form of the model.

5.1. Joint-torque-driven model

Given that the selected n generalised coordinates and generalised speeds are independent, the dynamic equations regulating the musculoskeletal system response are a collection of ordinary differential equations. The equations of motion are transformed into optimised code by employing the "Multibody Dynamic Exports" and "Optimised Code Generation" modules of MapleSim [102, 103]. Equation (10) represents the joint-torque-driven (MTG-excluded) dynamic model.

$$\mathbf{M}_{n\times n}\left(\boldsymbol{\theta}_{n\times 1}\right)\dot{\boldsymbol{\omega}}_{n\times 1} = \mathbf{F}_{n\times 1}\left(\boldsymbol{\omega}_{n\times 1}, \boldsymbol{\theta}_{n\times 1}\right) + \mathbf{Q}_{n\times 1} \tag{10}$$

where

n	the number of independent coordinates including the 6 absolute coordinates for the pelvis with respect to ground (3 translations, 3 rotations)
$\boldsymbol{\theta}$	the column matrix of generalized coordinates
$\boldsymbol{\omega}$	the column matrix of generalized speeds
$\mathbf{M}$	the mass matrix
$\mathbf{F}$	the right-hand side of the dynamic equations, which consist of Coriolis, centrifugal, and gravitational effects
$\mathbf{Q}$	external loads, including joint torques

5.2. Active-torque-driven model

With the introduction of the passive torque function from section 3.1, the active-torque-driven dynamic model is in the form of Equation (10). By using Equation (11), the active torques are transformed to human joint ideal torques. Basically, the activation-driven model incorporates Equations (10, 11).

$$\mathbf{Q}_{m\times 1} = \left[\tau_a + \tau_p\left(\boldsymbol{\theta}, \boldsymbol{\omega}\right)\right]_{m\times 1} \tag{11}$$

where

m $n-6$ or the number of human joints (excluding the 6 absolute coordinates for the pelvis with respect to ground (3 translations, 3 rotations))

5.3. Activation-signal-driven model

Equation (10) represents the activation-signal-driven (MTG-included) dynamic model. Equation (12), which is derivable from Equation (4), converts the activation signals of positive and negative directions into human joint torques. The activation-driven model merges Equations (10,12).

$$\mathbf{Q}_{m\times 1} = \left[\boldsymbol{a}^{+}\boldsymbol{\tau}_{\omega}^{+}\left(\boldsymbol{\omega}\right)\boldsymbol{\tau}_{\theta}^{+}\left(\boldsymbol{\theta}\right)\boldsymbol{\tau}_{0}^{+} + \boldsymbol{a}^{-}\boldsymbol{\tau}_{\omega}^{-}\left(\boldsymbol{\omega}\right)\boldsymbol{\tau}_{\theta}^{-}\left(\boldsymbol{\theta}\right)\boldsymbol{\tau}_{0}^{-} + \boldsymbol{\tau}_p\left(\boldsymbol{\theta}, \boldsymbol{\omega}\right)\right]_{m\times 1} \tag{12}$$

where

$^{+}$ the positive direction of joint
$^{-}$ the negative direction of the joint

5.4. Excitation-signal-driven model

As illustrated in Equation (13), adding the first-order differential equation of excitation-to-activation (established in Equation (9)) results in the introduction of a new state to the system. Some studies avoid this additional state by using a different formulation (such as the exponential gain formula), but their alternative strategy ignores the time delay between excitation and activation [83].

$$\begin{bmatrix} I_{2m\times 2m} & 0 \\ 0 & \mathbf{M}_{n\times n}\left(\boldsymbol{\theta}_{n\times 1}\right) \end{bmatrix} \begin{bmatrix} \dot{\boldsymbol{a}}_{2m\times 1} \\ \dot{\boldsymbol{\omega}}_{n\times 1} \end{bmatrix} = \begin{bmatrix} \boldsymbol{u2a}\left(\boldsymbol{a}_{2m\times 1}, \boldsymbol{u}_{2m\times 1}, t\right)_{2m\times 1} \\ \mathbf{F}_{n\times 1}\left(\boldsymbol{\omega}_{n\times 1}, \boldsymbol{\theta}_{n\times 1}\right) + \mathbf{Q}_{n\times 1} \end{bmatrix} \tag{13}$$

$$\mathbf{Q}_{m\times 1} = \left[\boldsymbol{a}^{+}\boldsymbol{\tau}_{\omega}^{+}\left(\boldsymbol{\omega}\right)\boldsymbol{\tau}_{\theta}^{+}\left(\boldsymbol{\theta}\right)\boldsymbol{\tau}_{0}^{+} + \boldsymbol{a}^{-}\boldsymbol{\tau}_{\omega}^{-}\left(\boldsymbol{\omega}\right)\boldsymbol{\tau}_{\theta}^{-}\left(\boldsymbol{\theta}\right)\boldsymbol{\tau}_{0}^{-} + \boldsymbol{\tau}_p\left(\boldsymbol{\theta}, \boldsymbol{\omega}\right)\right]_{m\times 1} \tag{14}$$

6. Simulation method

6.1. Inverse dynamic simulation

Inverse dynamics is the process of computing the forces, moments, activations, and excitations that emerge at particular joints after solving the torque-driven equations

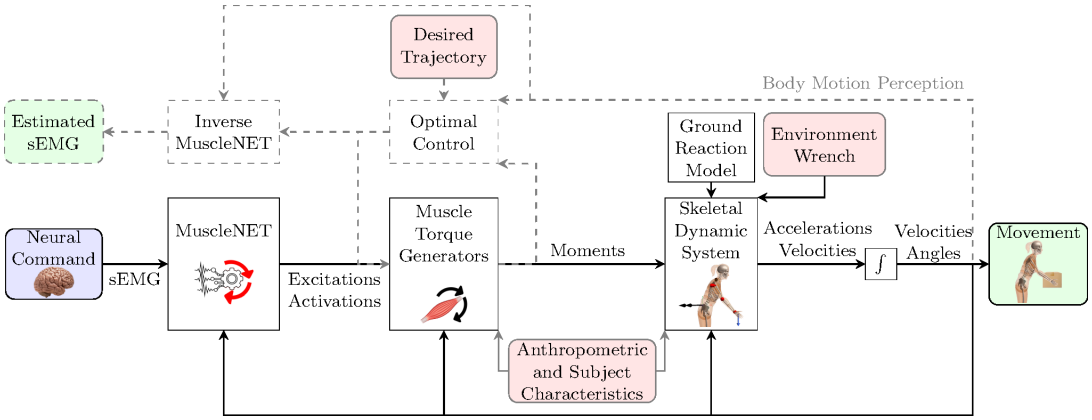

Figure 7.: Components of a typical musculoskeletal simulation within MapleSim Biomechanics are responsible for orchestrating movement through the interactions of neural, muscular, and skeletal systems. MapleSim Biomechanics encompasses computational models of these systems, enabling prediction and analysis of human movement. Neural commands in the form of excitations are directed towards the MTGs and can be estimated using either optimal controller models or experimental data, such as surface electromyography with the assistance of machine learning mapping electromyography to kinematic and dynamic biomechanical variables (MuscleNET) [82]. The MapleSim Biomechanics MTG models, which translate these excitations into biomechanical joint torque, incorporate features like passive torque, active torque angle scaling, and active torque angular velocity scaling that simulate the biomechanical behavior of the joint. These MTG models are established from experimental data. Additionally, MapleSim Biomechanics accounts for factors such as age, height, body mass, dominant side, athletic activity, and skin temperature to determine the peak joint strength of an individual [2],.

of motion (given in section 5.1) and MTG model [104]. For a single joint, the MTG models have various positive and negative torques. This over-actuation necessitates the elimination of actuation redundancy, mostly through optimisation techniques. To calculate positive and negative active MTG torques, static and dynamic optimisation are two variations employed. Static optimization is regarded as an inverse technique since it uses time-marching to optimise MTG torques, which implies that time frames are solved independently of each [11]. Once the positive and negative active MTG torques are calculated, the inverse dynamic simulation can determined the positive and negative MTG activation signals.

6.2. Forward dynamic simulation

Basically, the human CNS, which consists of the brain and spinal cord, regulates the movement of the body [105, 106]. The CNS concurrently maintains the kinetics and kinematics even in the presence of complex muscle dynamics and uncertain/unknown trajectories [106, 107]. According to experimental studies on human mobility [1, 108–110], the CNS organises human motions in an optimal way. Numerous research suggest that the CNS controls the human by minimising a cost function that may involve jerk [111], torque [112], muscle activation [98], metabolic energy [113], and muscle fatigue [114].

The CNS controls human movements through a sophisticated signal that involves two main processes: motion prediction and corrective command [106]. To achieve this, the CNS utilizes an internal model of the musculoskeletal system for feed-forward control, enabling motion prediction. Additionally, sensory organs provide feedback control, rectifying errors arising from model uncertainty, external disturbances, or unfamiliar environments. A method known as nonlinear model predictive control replicates this multi-purpose control system with a limited time horizon, integrating both feed-forward and feedback control [106] (see Figure 7). nonlinear model predictive control utilizes a learned internal model [115, 116] that emulates human dynamics to forecast optimal motion (feed-forward) and correct prediction errors (feedback) [106]. The evaluation of the ideal motion involves a cost function that considers joint angle errors ($\boldsymbol{\theta} - \boldsymbol{\theta}_\mathbf{d}$), joint angular velocity errors ($\boldsymbol{\omega} - \boldsymbol{\omega}_\mathbf{d}$), model inputs and their derivatives, as well as weights ($\mathbf{W}$). For the activation-signal-driven model with input $\boldsymbol{a}$, this cost function can be represented as Equation (15).

$$J = \int_0^{t_f} \left[\mathbf{W}_1^T \left(\boldsymbol{\theta} - \boldsymbol{\theta}_\mathbf{d}\right)^2 + \mathbf{W}_2^T \left(\boldsymbol{\omega} - \boldsymbol{\omega}_\mathbf{d}\right)^2 + \mathbf{W}_3^T \left(\boldsymbol{a}\right)^2 + \mathbf{W}_4^T \left(\dot{\boldsymbol{a}}\right)^2 \right] dt \tag{15}$$

$$\begin{aligned} \boldsymbol{\theta}_{min} \leq \boldsymbol{\theta} \leq \boldsymbol{\theta}_{max} \\ \boldsymbol{\omega}_{min} \leq \boldsymbol{\omega} \leq \boldsymbol{\omega}_{max} \\ \mathbf{0} \leq \boldsymbol{a} \leq \mathbf{1} \\ \dot{\boldsymbol{a}}_{min} \leq \dot{\boldsymbol{a}} \leq \dot{\boldsymbol{a}}_{max} \end{aligned} \tag{16}$$

The nonlinear model predictive control controller optimizes the cost function (15) considering the system dynamics presented in section 5 and the constraints outlined in Equation (16).

The excitation or activation of the musculoskeletal MTG model can be achieved through three methods:

i) A forward static optimization approach, which approximates the musculoskeletal system behavior by statically reducing a physiological cost functional (essentially a 1-step nonlinear model predictive control).
ii) A forward dynamic optimization approach, which models the musculoskeletal system behavior by dynamically minimizing a physiological cost functional.
iii) Utilizing experimental surface electromyography data from a subject, which can be mapped to MTG inputs using a machine learning model [82].

7. Model validation

We evaluate the model's performance by comparing the estimated moments at specific joints with the measured moments obtained during various predicted movements. The experimental study involves the use of dynamotor measurement devices, which restrict joint motion and enable the measurement of joint moments. During these tests, subjects are instructed to exert maximum flexion or extension against the device's resistance, and the resulting isometric and isokinetic torques are recorded. The maximum isometric test is conducted with zero joint velocity, while the isokinetic test is performed with the dynamotor measurement system controlling the joint velocity. To simulate the isometric and isokinetic tests, we use the MapleSim Biomechanics model and forward dynamics. When determining the maximum isometric moment-generating

capability, we consider the model's maximum activation for MTG.

As mentioned in section 3.2, the peak isometric torque at the joints is influenced by various factors, including age [20, 22, 23], height [20, 24, 26], body mass [20, 24, 25], as well as sex, dominant side [27], athletic activity [63], and skin temperature [32].

7.1. Isometric test

The maximum isometric joint moments obtained from the MapleSim Biomechanics model incorporate data from numerous published experiments. As the validation experiments utilized in these publications involved a small number of subjects (fewer than 10), our comparison with the experimental literature concentrates on identifying trends and patterns in the maximum isometric joint torques.

The trend of the maximum isometric torques produced by the hip flexor (HFE) as a function of flexion angle aligns well with the data reported by previous studies [45, 57, 117, 118] within the ROM of the hip flexor (see Figure 8a). Specifically, the maximum torque of the hip flexor decreases as the hip flexion angle increases, consistent with the provided experimental data.

Regarding the maximum isometric moment generated by the HAA, Figure 8b demonstrates a pattern that corresponds to the study conducted by Venter [47] for the ROM of the HAA. However, it does not precisely match the findings of Welsh et al. [119], Cahalan et al. [120] or Neumann et al. [121].

Figure 8c shows similar trends between the estimated isometric torque of the HIER by the MapleSim Biomechanics model and the experimental data from Guilhem et al. [45], Lindsay et al. [49] and Gupta et al. [122]. The MapleSim Biomechanics model generates the HIER torque at approximately 5^o hip internal rotation angle, which aligns with the experimental data.

The model reflects the observed trends in the literature data for KFE strength, as the knee extension angle increases (see Figure 9a). The KFE torque reaches its peak at approximately -65^o rotation, similar to the experimental data reported by Guilhem et al. [45] and Knapik et al. [123]. Furthermore, the model successfully reproduces the experimental trend in ADPF strength as the ankle dorsiflexion angle changes (see Figure 9d). The ADPF torque peaks at approximately -10^o rotation angle, which aligns with the experimental data. Additionally, the model's moment-generating capacity for AAA and AEI decreases at a rate consistent with the findings in the literature [50, 53, 126], as the ankle angle increases (see Figure 9c & d).

7.2. Isokinetic test

The study compares the maximum isokinetic joint moments calculated using the MapleSim Biomechanics model with experimental data from the literature, as depicted in Figure 11 and 10. However, due to differences in subject types, not only the amplitude of the isokinetic torque but also the maximum possible torque for the highest reported angular velocity is not compared in this research.

As shown in Figure 11, for the concentric isokinetic test of joints, both the experimental and MapleSim Biomechanics estimations demonstrate a decrease in torques as the angular velocity increases [64, 120, 124, 127–138]. Similarly, for the eccentric isokinetic test, both the experimental data and MapleSim Biomechanics simulation show an increase in torques with an increasing angular velocity. In conclusion, the maximum isokinetic torque of joints estimated by the MapleSim Biomechanics model

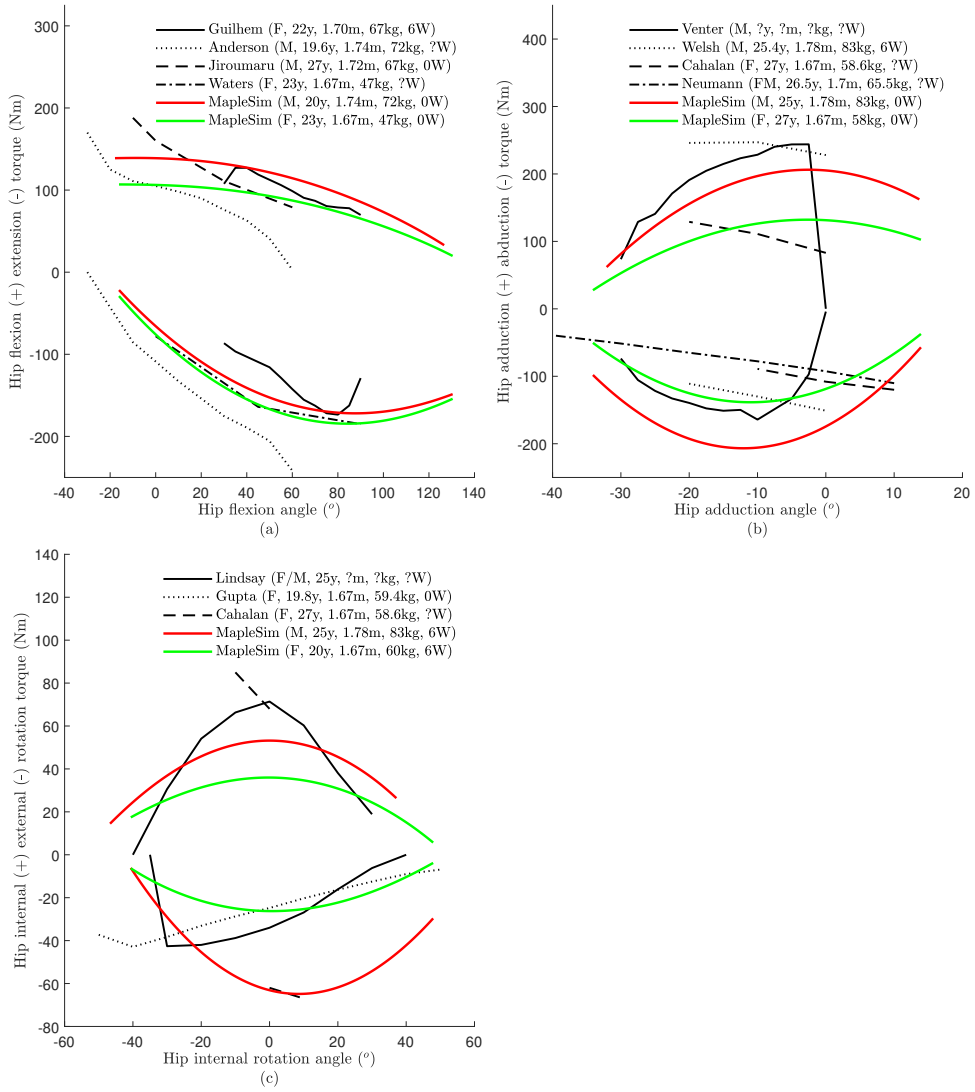

Figure 8.: Maximum isometric torque generated by (a) hip flexors (+) and extensors (-) versus hip flexion, (b) hip adductors (+) and abductors (-) versus hip adduction, and (c) hip internal (+) and external (-) axial rotator versus hip internal rotation. The model estimates are highlighted in colored solid lines and are compared to experimental data from Guilhem et al. [45], Venter [47], Lindsay et al. [49], Anderson et al. [57], Jiroumaru et al. [117], Waters et al. [118], Welsh et al. [119], Cahalan et al. [120], Neumann et al. [121] and Gupta et al. [122]. HFE, HAA, and HIER were determined with a straight leg in the neutral position. M: Male, F: Female, Height is in meter (m), Weight is in kilograms (kg), number of workout sessions per week shown with W.

follows the same trend as the experimental data reported in the literature.

8. Discussion

We developed a musculoskeletal model for the lower body of humans, including the hip, knee and ankle joints. The model is based on average experimental data for biome-

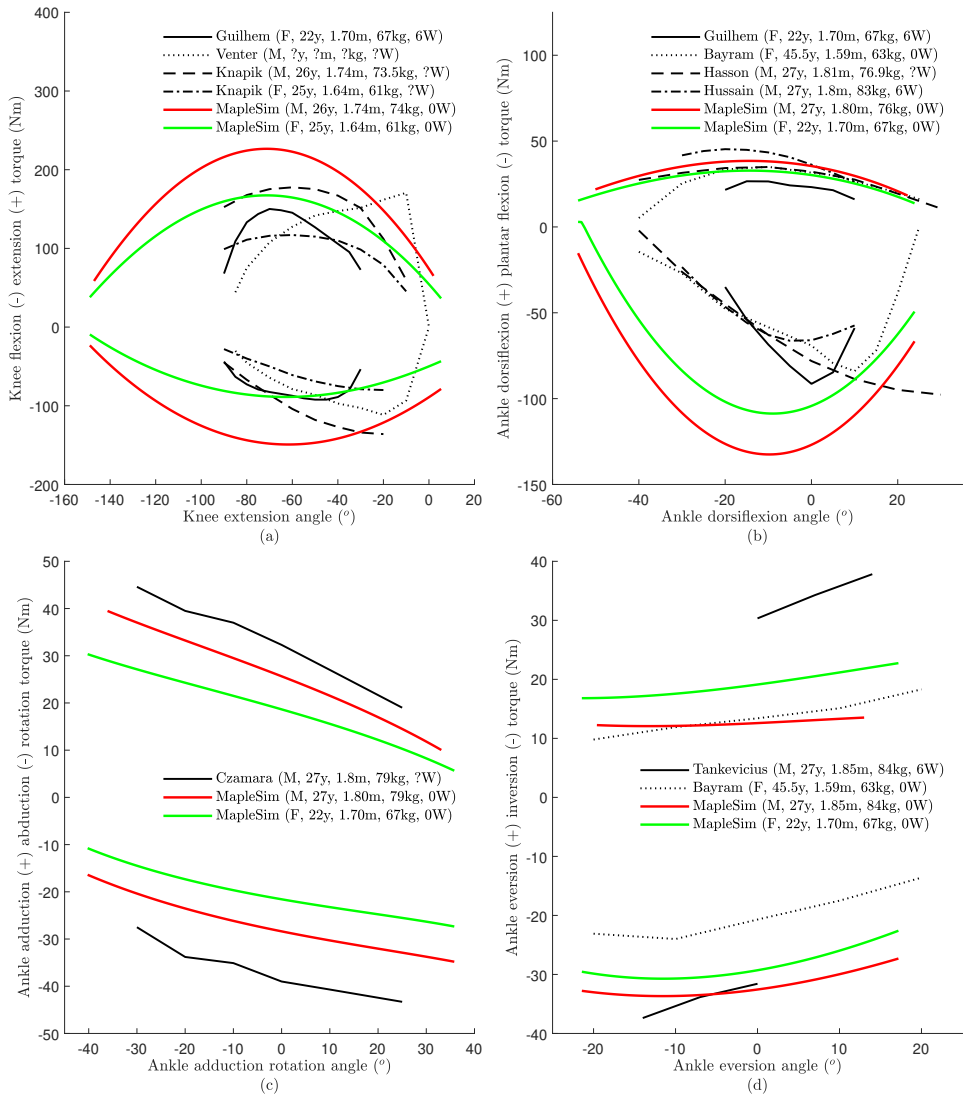

Figure 9.: Maximum isometric torque generated by (a) knee flexors (-) and extensors (+) versus knee extension rotation, (b) ankle dorsiflexors (+) and plantar flexors (-) versus ankle dorsiflexion rotation, (c) ankle adductors (+) and abductors (-) versus ankle adduction rotation, and (d) ankle eversion (+) and inversion (-) versus ankle eversion rotation. The model estimates are highlighted in colored solid lines and are compared to experimental data from our test (mentioned in section 3.3), Guilhem et al. [45], Venter [47], Bayram et al. [50], Czamara et al. [53], Knapik et al. [123], Hasson et al. [124], Hussain and Frey-Law [125], Tankevicius et al. [126] and Bayram et al. [50]. M: Male, F: Female, Height is in meter (m), Weight is in kilograms (kg), number of workout sessions per week shown with W.

chanics, such as segment and joint properties (dimensions, inertia, maximum joint torque, maximum ROM, maximum angular velocity, and maximum isometric torque-angle profile). The model can be customized according to subject body characteristics: sex, age, body mass, height, dominant side, physical activity, and skin temperature.

A significant contribution of this study is the provision of comprehensive data for

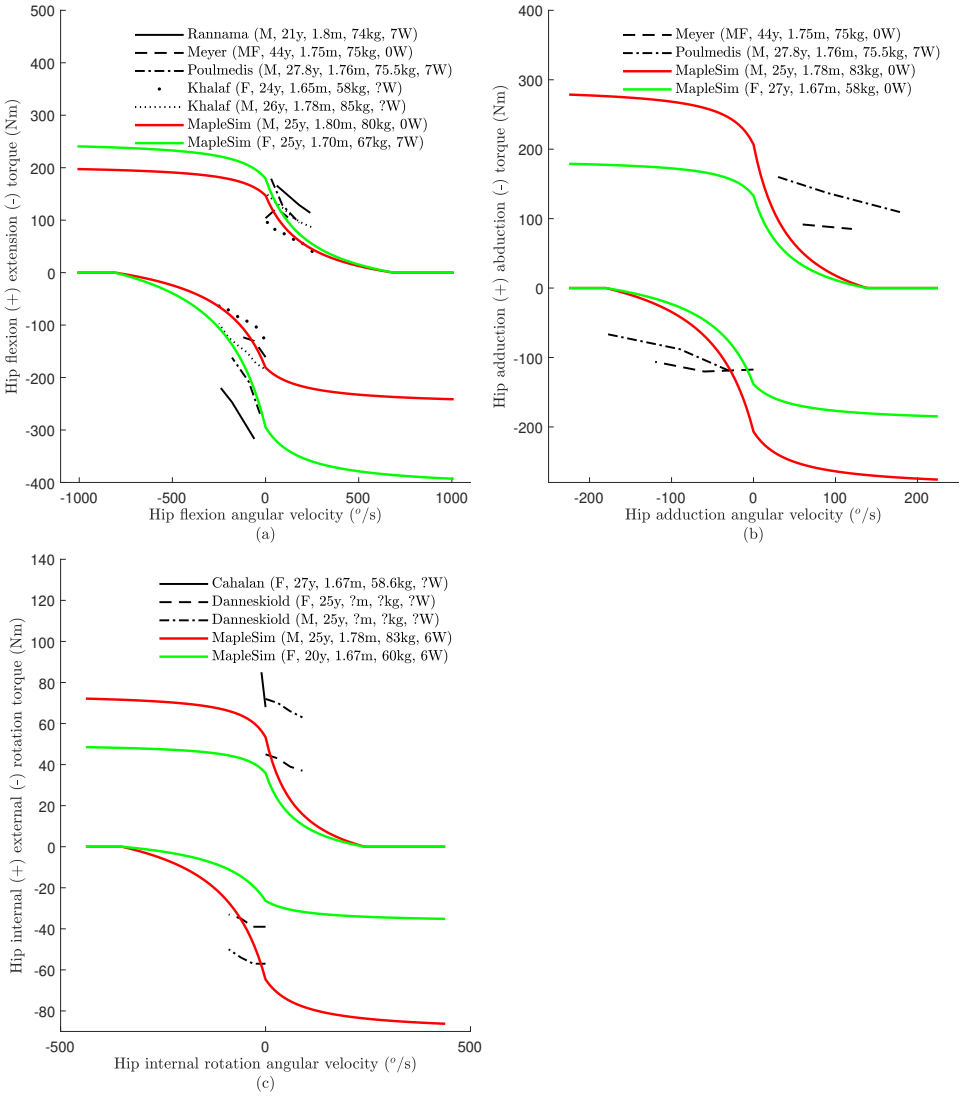

Figure 10.: Maximum isokinetic torque generated by (a) hip flexors (+) and extensors (-) versus hip flexion angular velocity, (b) hip adductors (+) and abductors (-) versus hip adduction angular velocity, and (c) hip internal (+) and external (-) axial rotator versus hip internal angular velocity. The model estimates are highlighted in colored solid lines and are compared to experimental data from our test (mentioned in section 3.3), Khalaf et al. [64], Cahalan et al. [120], Rannama et al. [127], Meyer et al. [128], Poulmedis [129] and Danneskiold-Samsoe et al. [130]. M: Male, F: Female, Height is in meter (m), Weight is in kilograms (kg), number of workout sessions per week shown with W.

constructing a mathematical model. The information presented in Table 3, Table 4, and Table 5, along with the equations provided, offer ample resources for developing a dynamic model. Researchers can concentrate on the specific joint of interest, disregarding data related to non-targeted joints.

To the best of our knowledge, our model stands out due to its broad scope and comprehensive nature in accommodating a wider range of anthropocentric variables

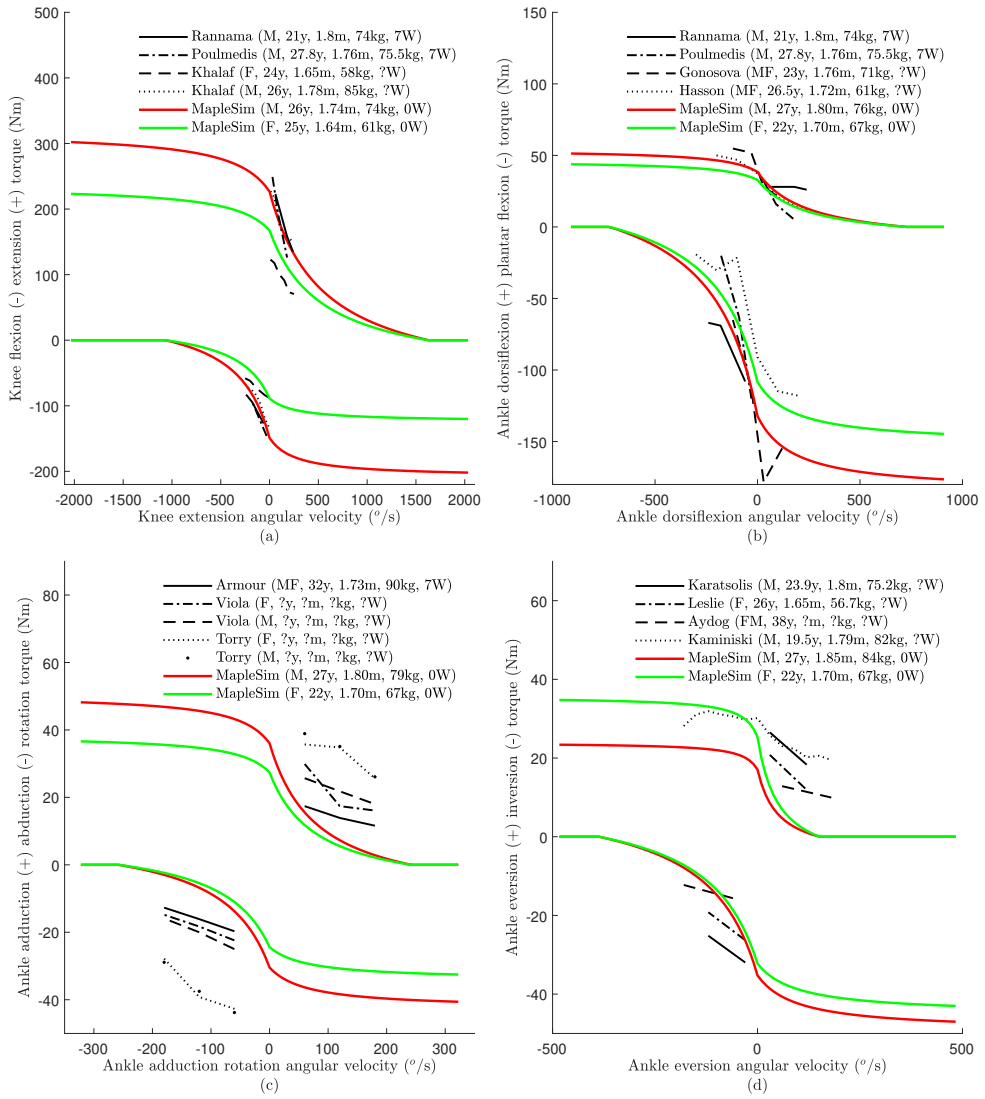

Figure 11.: Maximum isokinetic torque generated by (a) knee flexors (-) and extensors (+) versus knee extension angular velocity, (b) ankle dorsiflexors (+) and plantar flexors (-) versus ankle dorsiflexion angular velocity, (c) ankle adductors (+) and abductors (-) versus ankle adduction angular velocity, (d) ankle eversion (+) and inversion (-) versus ankle eversion angular velocity. The model estimates are highlighted in colored solid lines and are compared to experimental data from our test (mentioned in section 3.3), Khalaf et al. [64], Hasson et al. [124], Rannama et al. [127], Poulmedis [129], Gonosova et al. [131], Armour et al. [132], Viola et al. [133], Torry et al. [134], Karatsolis et al. [135], Leslie et al. [136], Aydog et al. [137] and Kaminski et al. [138]. M: Male, F: Female, Height is in meter (m), Weight is in kilograms (kg), number of workout sessions per week shown with W.

compared to other presented musculoskeletal models. Furthermore, our model has undergone verification and validation. The data used for constructing this comprehensive model is drawn from literature sources involving multiple subjects, in contrast to the subject-specific models proposed in previous works such as [17, 139].

Unlike most musculoskeletal models, which lack validation for all ROMs [19, 139–141], we have constructed and verified our model using maximum ROM data from the literature. Additionally, to ensure accuracy, the average maximum angular velocity from the literature is utilized to limit the maximum isokinetic joint torque in concentric motion, and the results are compared against experimental literature.

For both female and male subjects, the maximum joint torque values are adopted from the literature [19, 20, 141]. The isometric joint torque-angle pattern is modeled using literature data [19, 24, 139, 140], or in some cases, our own experimental measurements. To develop the isokinetic torque-angular-speed profile, we employ literature data from [10, 39, 76, 77, 80] along with the previously mentioned average maximum angular velocity.

The skeletal dynamic model can be tuned for sex, body mass, and body height since they influence the anatomical locations, the COMs, and inertia parameters [34, 35]. The biomechanical joint torque is also subject-specific. The variations in peak torque concerning age [20, 22, 23], height [20, 24, 26], body mass [20, 24, 25], dominant side [27], activity level [63], and skin temperature are modeled based on the literature data. The maximum joint ROM can be affected by sex differences in passive torque function. Additionally, age impacts the excitation-to-activation delay, as reported by [86].

8.1. Applications

This biomechanical model has many potential uses in different fields such as: human movement simulation (joint torques, ROM), biomechatronics, ergonomics and usability studies, predictive simulation of daily activities (reaching, walking, sitting, etc), clinical practice, human-device interactions, sports engineering, and medical and assistive device development/control. Some of these uses are explained in more detail below.

The use of subject-specific torque-driven computer models in studying human movement has yielded valuable insights into optimal athletic technique [142]. By simulating athletic dynamics, computer simulation provides a useful means of investigating various issues such as equipment design, injury prevention, and motor control methods, all of which contribute to improved sports performance [37]. Researchers can modify significant circumstances and parameters through this interface, allowing for predictive simulation trials that do not require actual experiments. Multibody computer simulation has been employed in the study of athletic performance across a range of activities, including golf and track cycling [37].

The development of new medical and assistive devices can be expedited and made safer through the use of predictive multibody dynamic simulations. Recently the Food and Drug Administration approved the use of computer simulation to enhance the design of medical devices [143]. These simulations have been applied to various devices such as orthoses, prostheses, and wearable exoskeleton robotics [1, 14]. To design and control biomechatronic devices, including exoskeletons, prostheses, and rehabilitation systems, it is necessary to incorporate models that account for human interaction [5, 6, 14, 144]. These models are integrated into computer simulations [4, 143], and the human biomechanical model can be used to control robotic devices based on modeling [4, 13, 82].

8.2. Limitations

The main weakness of MTG models is not providing information about muscle tension [1]. Anatomically detailed muscle models are needed to evaluate joint reaction force/torque as well as the muscle tensions. Our model uses MTGs instead of an anatomical-detailed model because of their ability to mimic the muscle group torque impact on the targeted joint. It should be noted that without direct verification of parameters for the anatomical-detailed model, the estimated muscle tension cannot be trusted. Our model has a wide range of applications in sports and biomechatronics analysis but is not suitable for muscle injury analysis.

The literature does not provide some parameters for all joints; therefore, the same constant value was considered for all of them. In the future, measuring this information with a high number of subjects can increase the accuracy of the model. For example, the impact of workout on the maximum joint angular velocity and the ratio of the maximum eccentric isokinetic torque (τ_m) over the maximum isometric torque (τ_0) can be studied in future.

A gap exists in the electromyography to MTG excitation mapping when using this model in electromyography-driven simulation, as shown in Figure 7. New opportunities for developing a machine learning mapping according to the MuscleNET model [82, 145] can be created by having experimental electromyography data.

The monoarticular assumption of muscles is used to model the joint torque [56], but this approach is not always accurate. The accuracy of these models can be improved by experimentally investigating the biarticular muscles and their impact on the MTG model [142, 146, 147].

In this study, the knee was characterized as a single DoF joint. However, considering the contribution of ligaments to stability across multiple DoF within the complex dynamics of knee motion [148], it is imperative to expand the consideration of multiple DoF when conducting motion studies to enhance the precision and accuracy of knee biomechanical analyses.

9. Conclusion

We developed a lower body model of the musculoskeletal system that can be adjusted for different individuals. The model has 20 DoFs controlled by 28 MTGs and is based on data from previous studies. The model can be customized according to various factors such as sex, age, body mass, height, dominant side, physical activity, and skin temperature. We validated the model by comparing the maximal isometric and isokinetic torque and workspace with existing literature. This model can be used for various applications such as sports analysis, ergonomics, daily activities, human-device interaction, and medical and assistive devices.

Abbreviation(s)

AAA ankle adduction/abduction.
ADPF ankle dorsiflexion/plantar flexion.
AEI ankle eversion/inversion.
CNS central nervous system.
COM center of mass.
DoF degree of freedom.

HAA hip adduction/abduction.
HFE hip flexion/extension.
HIER hip internal/external rotation.
ISB International Society of Biomechanics.
KFE knee flexion/extension.
MTG muscle torque generator.
MuscleNET machine learning mapping electromyography to kinematic and dynamic biomechanical variables.
ROM range of motion.

Acknowledgement(s)

This research is supported by funding from the Canada Research Chairs Program and the Natural Sciences and Engineering Research Council of Canada.

Notes on contributor(s)

A.N. and J.M. conceived and designed the research. A.N. and J.M. read and selected the references. A.N. coded the models, simulations, did validations, wrote the first draft. A.N. and J.M. revised the manuscript. J.M. secured funding for this research. All authors reviewed the manuscript.

References

[1] Febrer-Nafría M, Nasr A, Ezati M, Brown P, Font-Llagunes JM, McPhee J (2022) Predictive multibody dynamic simulation of human neuromusculoskeletal systems: A review. Multibody System Dynamics pp 1–41,

[2] Nasr A, Hashemi A, McPhee J (2023) Scalable musculoskeletal model for dynamic simulations of upper body movement. Computer Methods in Biomechanics and Biomedical Engineering pp 1–32,

[3] Shourijeh MS, Mehrabi N, McPhee JJ, Fregly BJ (2020) Advances in musculoskeletal modeling and their application to neurorehabilitation. Frontiers in Neurorobotics 14:65,

[4] Nasr A, Laschowski B, McPhee J (2021) Myoelectric control of robotic leg prostheses and exoskeletons: A review. In: Proceedings of the ASME International Design Engineering Technical Conferences & Computers and Information in Engineering Conference, ASME, Online, Virtual, vol 85444, pp 2021–69203,

[5] Nasr A, Bell S, McPhee J (2023) Optimal design of active-passive shoulder exoskeletons: A computational modeling of human-robot interaction. Multibody System Dynamics 57:73–106,

[6] Nasr A, Ferguson S, McPhee J (2022) Model-based design and optimization of passive shoulder exoskeletons. Journal of Computational and Nonlinear Dynamics 17(5):051004,

[7] Laschowski B, Razavian RS, McPhee J (2021) Simulation of stand-to-sit biomechanics for robotic exoskeletons and prostheses with energy regeneration. IEEE Transactions on Medical Robotics and Bionics 3(2):455–462,

[8] Ghannadi B, Razavian RS, McPhee J (2018) Upper extremity rehabilitation robots: A survey. In: Handbook of Biomechatronics, Elsevier, San Diego, CA, USA, chap 9, pp 319–353,

[9] Cardona M, García Cena CE (2019) Biomechanical analysis of the lower limb: A full-body musculoskeletal model for muscle-driven simulation. IEEE Access 7:92709–92723,

[10] McNally W, McPhee J (2018) Dynamic optimization of the golf swing using a six degree-of-freedom biomechanical model. In: Proceedings, MDPI, Brisbane, Queensland, Australia, vol 2, p 243,

[11] Ezati M, Ghannadi B, McPhee J (2019) A review of simulation methods for human

movement dynamics with emphasis on gait. Multibody System Dynamics 47(3):265–292,
[12] Razavian RS, Ghannadi B, McPhee J (2019) On the relationship between muscle synergies and redundant degrees of freedom in musculoskeletal systems. Frontiers in Computational Neuroscience 13:23,
[13] Nasr A, Hashemi A, McPhee J (2022) Model-based mid-level regulation for assist-as-needed hierarchical control of wearable robots: A computational study of human-robot adaptation. Robotics 11(1):20,
[14] Nasr A, McPhee J (2022) Biarticular MuscleNET: A machine learning model of biarticular muscles. In: Proceedings of the North American Congress on Biomechanics, Ottawa, Canada
[15] Jansen C, McPhee J (2020) Predictive dynamic simulation of Olympic track cycling standing start using direct collocation optimal control. Multibody System Dynamics 49(1):53–70,
[16] Destarac MA, García Cena CE, Saltarén Pazmiño RJ, Reyes Urbina MJ, López López J, Gómez RE (2016) Modeling and simulation of upper brachial plexus injury. IEEE Systems Journal 10(3):912–921,
[17] Cazzola D, Holsgrove TP, Preatoni E, Gill HS, Trewartha G (2017) Cervical spine injuries: A whole-body musculoskeletal model for the analysis of spinal loading. PLoS ONE 12(1):e0169329,
[18] Zhang L, Liu G, Yan Y, Han B, Li H, Ma J, Wang X (2022) A subject-specific musculoskeletal model to predict the tibiofemoral contact forces during daily living activities. Computer Methods in Biomechanics and Biomedical Engineering
[19] Kumar S (1996) Isolated planar trunk strengths measurement in normals: Part III - Results and database. International Journal of Industrial Ergonomics 17(2):103–111,
[20] Harbo T, Brincks J, Andersen H (2012) Maximal isokinetic and isometric muscle strength of major muscle groups related to age, body mass, height, and sex in 178 healthy subjects. European Journal of Applied Physiology 112(1):267–275,
[21] Gallagher MA, Cuomo F, Polonsky L, Berliner K, Zuckerman JD (1997) Effects of age, testing speed, and arm dominance on isokinetic strength of the elbow. Journal of Shoulder and Elbow Surgery 6(4):340–346,
[22] Staudte HW, Duhr N (1994) Age- and sex-dependent force-related function of the cervical spine. European Spine Journal 3(3):155–161,
[23] Yassierli, Nussbaum MA, Iridiastadi H, Wojcik LA (2007) The influence of age on isometric endurance and fatigue is muscle dependent: A study of shoulder abduction and torso extension. Ergonomics 50(1):26–45,
[24] Jordan A, Mehlsen J, Bülow PM, Ostergaard K, Danneskiold-Samsee B (1999) Maximal isometric strength of the cervical musculature in 100 healthy volunteers. Spine 24(13):1343–1348,
[25] Okada T, Hakkaku T, Iwai K, Nakazato K (2021) Weight category-dependent trunk muscle strength and its relation with LBP in elite judokas. Sports Medicine International Open 05(01):E14–E21,
[26] Roberson JM, Witt P, Gross MT (1997) A comparison of trunk extensor strength and squat lifting ability. Journal of Orthopaedic and Sports Physical Therapy 25(2):137–144,
[27] Zuzgina O, Wdowski MM (2019) Asymmetry of dominant and non-dominant shoulders in university level men and women volleyball players. Human Movement 20(4):19–27,
[28] Söderman K, Bergström E, Lorentzon R, Alfredson H (2000) Bone mass and muscle strength in young female soccer players. Calcified Tissue International 67(4):297–303,
[29] Close R, Hoh JF (1968) Influence of temperature on isometric contractions of rat skeletal muscles. Nature 217(5134):1179–1180,
[30] Racinais S, Oksa J (2010) Temperature and neuromuscular function. Scandinavian Journal of Medicine and Science in Sports 20(SUPPL. 3):1–18,
[31] Mallette MM, Green LA, Hodges GJ, Fernley RE, Gabriel DA, Holmes MW, Cheung SS (2019) The effects of local muscle temperature on force variability. European Journal of Applied Physiology 119(5):1225–1233,
[32] Ekblom B, Bergh U (1979) Influence of muscle temperature on maximal muscle strength and power output in human skeletal muscles. Acta Physiologica Scandinavica 107:33–37,
[33] Lloyd A, Hodder S, Havenith G (2015) The interaction between peripheral and central fatigue at different muscle temperatures during sustained isometric contractions.

American Journal of Physiology - Regulatory Integrative and Comparative Physiology 309(4):R410–R420,
[34] Dumas R, Chèze L, Verriest JP (2007) Adjustments to McConville et al. and Young et al. body segment inertial parameters. Journal of Biomechanics 40(3):543–553,
[35] McConville JT, Churchill T, Kaleps I, Clauser CE, Cuzzi J (1980) Anthropometric relationships of body and body segment moments of inertia. Tech. rep., Air Force Aerospace Medical Research Laboratory, Aerospace Medical Division, Dayton, OH, USA
[36] Winters JM (1990) Hill-based muscle models: A systems engineering perspective. In: Multiple Muscle Systems, Springer, New York, NY, USA, chap 5, pp 69–93,
[37] Inkol KA, Brown C, McNally W, Jansen C, McPhee J (2020) Muscle torque generators in multibody dynamic simulations of optimal sports performance. Multibody System Dynamics 50(4):435–452,
[38] Nasr A (2022) Design, dynamics, and control of active-passive upper-limb exoskeleton robots. PhD thesis, University of Waterloo, Waterloo, ON, Canada
[39] Brown C, McNally W, McPhee J (2020) Optimal control of joint torques using direct collocation to maximize ball carry distance in a golf swing. Multibody System Dynamics 50(3):323–333,
[40] Wu G, Siegler S, Allard P, Kirtley C, Leardini A, Rosenbaum D, Whittle M, D'Lima DD, Cristofolini L, Witte H, Schmid O, Stokes I (2002) ISB recommendation on definitions of joint coordinate system of various joints for the reporting of human joint motion - Part I: Ankle, hip, and spine. Journal of Biomechanics 35(4):543–548,
[41] Durkin JL, Dowling JJ (2003) Analysis of body segment parameter differences between four human populations and the estimation errors of four popular mathematical models. Journal of Biomechanical Engineering 125(4):515–522,
[42] Pavol MJ, Owings TM, Grabiner MD (2002) Body segment inertial parameter estimation for the general population of older adults. Journal of Biomechanics 35(5):707–712,
[43] Moromizato K, Kimura R, Fukase H, Yamaguchi K, Ishida H (2016) Whole-body patterns of the range of joint motion in young adults: Masculine type and feminine type. Journal of Physiological Anthropology 35(1):1–12,
[44] Jessop DM, Pain MT (2016) Maximum velocities in flexion and extension actions for sport. Journal of Human Kinetics 50(1):37–44,
[45] Guilhem G, Giroux C, Couturier A, Chollet D, Rabita G (2014) Mechanical and muscular coordination patterns during a high-level fencing assault. Medicine and Science in Sports and Exercise 46(2):341–350,
[46] Ibrahim R, Kingma I, de Boode V, Faber GS, van Dieën JH (2020) Angular velocity, moment, and power analysis of the ankle, knee, and hip joints in the goalkeeper's diving save in football. Frontiers in Sports and Active Living 2,
[47] Venter MRMR (2000) Physiological changes associated with lateral movement training of netball players. PhD thesis, Stellenbosch University, Stellenbosch, South Africa
[48] Matsuda Y, Kaneko M, Sakurai Y, Akashi K, Yasuo S (2021) Three-dimensional lower-limb kinematics during undulatory underwater swimming. Sports Biomechanics
[49] Lindsay DM, Maitland ME, Lowe RC, Kane TJ (1992) Comparison of isokinetic internal and external hip rotation torques using different testing positions. Journal of Orthopaedic and Sports Physical Therapy 16(1):43–50,
[50] Bayram S, Kendirci ASS, Kıral DD, Sahinkaya T, Ekinci M, Batıbay SG, Akgul T, Sahinkaya T, Ekinci M, Batıbay SG, Akgul T (2020) Isokinetic Strength Comparison of Tuberosity Fractures of the Proximal Fifth Metatarsal Treated With Elastic Bandage vs Cast. Foot and Ankle International 41(6):674–682,
[51] Grimston SK, Nigg BM, Hanley DA, Engsberg JR (1993) Differences in Ankle Joint Complex Range of Motion as a Function of Age. Foot & Ankle International 14(4):215–222,
[52] Zhang S, Wortley M, Chen Q, Freedman J (2009) Efficacy of an ankle brace with a subtalar locking system in inversion control in dynamic movements. Journal of Orthopaedic and Sports Physical Therapy 39(12):875–883,
[53] Czamara A, Szuba L, Krzeminska A, Tomaszewski W, Wilk-Franczuk M, Szuba L, Krzeminska A, Tomaszewski W, Wilk-Franczuk M (2011) Effect of physiotherapy on the strength of tibial internal rotator muscles in males after anterior cruciate ligament reconstruction (ACLR). Medical Science Monitor 17(9),
[54] Yeadon MR, King MA, Wilson C (2006) Modelling the maximum voluntary joint

torque/angular velocity relationship in human movement. Journal of Biomechanics 39(3):476–482,
[55] Inkol KA, McPhee J (2020) Assessing control of fixed-support balance recovery in wearable lower-limb exoskeletons using multibody dynamic modelling. In: Proceedings of the IEEE RAS and EMBS International Conference on Biomedical Robotics and Biomechatronics, IEEE, New York, NY, USA, pp 54–60,
[56] Lewis MG, Yeadon MR, King MA (2018) The effect of accounting for biarticularity in hip flexor and hip extensor joint torque representations. Human Movement Science 57:388–399,
[57] Anderson DE, Madigan ML, Nussbaum MA (2007) Maximum voluntary joint torque as a function of joint angle and angular velocity: Model development and application to the lower limb. Journal of Biomechanics 40(14):3105–3113,
[58] Hoang PD, Gorman RB, Todd G, Gandevia SC, Herbert RD (2005) A new method for measuring passive length-tension properties of human gastrocnemius muscle in vivo. Journal of Biomechanics 38(6):1333–1341,
[59] Yoon YS, Mansour JM (1982) The passive elastic moment at the hip. Journal of Biomechanics 15(12):905–910,
[60] Yamaguchi GT (2006) Dynamic modeling of musculoskeletal motion: A vectorized approach for biomechanical analysis in three dimensions, 1st edn. Springer, Boston, MA, USA,
[61] Lanshammar K, Ribom EL (2011) Differences in muscle strength in dominant and non-dominant leg in females aged 20-39 years - A population-based study. Physical Therapy in Sport 12(2):76–79,
[62] Guette M, Gondin J, Martin A (2005) Time-of-day effect on the torque and neuromuscular properties of dominant and non-dominant quadriceps femoris. Chronobiology International 22(3):541–558,
[63] Gentil P, Fischer B, Martorelli AS, Lima RM, Bottaro M (2015) Effects of equal-volume resistance training performed one or two times a week in upper body muscle size and strength of untrained young men. Journal of Sports Medicine and Physical Fitness 55(3):144–149
[64] Khalaf KA, Parnianpour M, Karakostas T (2001) Three dimensional surface representation of knee and hip joint torque capability. Biomedical Engineering - Applications, Basis and Communications 13(2):53–65,
[65] Lopez-Valenciano A, Ayala F, De Ste Croix M, Barbado D, Vera-Garcia FJ (2019) Different neuromuscular parameters influence dynamic balance in male and female football players. Knee Surgery, Sports Traumatology, Arthroscopy 27(3):962–970,
[66] Johnson S, Hoffman M (2010) Isometric hip-rotator torque production at varying degrees of hip flexion. Journal of Sport Rehabilitation 19(1):12–20,
[67] Lategan L (2011) Isokinetic norms for ankle, knee, shoulder and forearm muscles in young South African men. Isokinetics and Exercise Science 19(1):23–32,
[68] Ottaviani RA, Ashton-Miller JA, Wojtys EM (2001) Inversion and Eversion Strengths in the Weightbearing Ankle of Young Women. The American Journal of Sports Medicine 29(2):219–225,
[69] Ottaviani RA, Ashton-Miller JA, Kothari SU, Wojtys EM (1995) Basketball Shoe Height and the Maximal Muscular Resistance to Applied Ankle Inversion and Eversion Moments. The American Journal of Sports Medicine 23(4):418–423,
[70] Kiriyama S, Sato H, Takahira N (2009) Gender differences in rotation of the shank during single-legged drop landing and its relation to rotational muscle strength of the knee. American Journal of Sports Medicine 37(1):168–174,
[71] Stoffel KK, Nicholls RL, Winata AR, Dempsey AR, Boyle JJ, Lloyd DG (2010) Effect of ankle taping on knee and ankle joint biomechanics in sporting tasks. Medicine and Science in Sports and Exercise 42(11):2089–2097,
[72] Forrester SE, Yeadon MR, King MA, Pain MT (2011) Comparing different approaches for determining joint torque parameters from isovelocity dynamometer measurements. Journal of Biomechanics 44(5):955–961,
[73] Haering D, Pontonnier C, Bideau N, Nicolas G, Dumont G (2019) Using torque-angle and torque-velocity models to characterize elbow mechanical function: Modeling and applied aspects. Journal of Biomechanical Engineering 141(8):084501,
[74] King MA, Wilson C, Yeadon MR (2006) Evaluation of a torque-driven model of jumping

for height. Journal of Applied Biomechanics 22(4):264–274,
[75] Alexander RM (1990) Optimum take-off techniques for high and long jumps. Philosophical transactions of the Royal Society of London Series B, Biological sciences 329(1252):3–10,
[76] Dudley GA, Harris RT, Duvoisin MR, Hather BM, Buchanan P (1990) Effect of voluntary vs. artificial activation on the relationship of muscle torque to speed. Journal of Applied Physiology 69(6):2215–2221,
[77] van Soest AJ, Bobbert MF (1993) The contribution of muscle properties in the control of explosive movements. Biological Cybernetics 69(3):195–204,
[78] Sprigings EJ (1986) Simulation of the force enhancement phenomenon in muscle. Computers in Biology and Medicine 16(6):423–430,
[79] Katz B (1939) The relation between force and speed in muscular contraction. Journal of Physiology 96(1):45–64,
[80] MacKenzie SJ, Sprigings EJ (2009) A three-dimensional forward dynamics model of the golf swing. Sports Engineering 11(4):165–175,
[81] Romero F, Alonso FJ (2016) A comparison among different Hill-type contraction dynamics formulations for muscle force estimation. Mechanical Sciences 7(1):19–29,
[82] Nasr A, Bell S, He J, Whittaker RL, Jiang N, Dickerson CR, McPhee J (2021) MuscleNET: Mapping electromyography to kinematic and dynamic biomechanical variables. Journal of Neural Engineering 18(4):0460d3,
[83] Buchanan TS, Lloyd DG, Manal K, Besier TF (2004) Neuromusculoskeletal modeling: Estimation of muscle forces and joint moments and movements from measurements of neural command. Journal of Applied Biomechanics 20(4):367–395,
[84] Meyer AJ (2016) Prediction of optimal rehabilitation outcomes post-stroke. PhD thesis, University of Florida, Gainesville, FL, USA
[85] Rockenfeller R, Günther M, Schmitt S, Götz T (2015) Comparative sensitivity analysis of muscle activation dynamics. Computational and Mathematical Methods in Medicine 2015:1–16,
[86] Thelen DG (2003) Adjustment of muscle mechanics model parameters to simulate dynamic contractions in older adults. Journal of Biomechanical Engineering 125(1):70–77,
[87] Mombaur K, Ho Hoang KL (2017) How to best support sit to stand transfers of geriatric patients: Motion optimization under external forces for the design of physical assistive devices. Journal of Biomechanics 58:131–138,
[88] Febrer-Nafría M, Pallarès-López R, Fregly BJ, Font-Llagunes JM (2021) Prediction of three-dimensional crutch walking patterns using a torque-driven model. Multibody System Dynamics 51(1):1–19,
[89] Serrancoli G, Falisse A, Dembia C, Vantilt J, Tanghe K, Lefeber D, Jonkers I, De Schutter J, De Groote F (2019) Subject-Exoskeleton Contact Model Calibration Leads to Accurate Interaction Force Predictions. IEEE transactions on neural systems and rehabilitation engineering : a publication of the IEEE Engineering in Medicine and Biology Society 27(8):1597–1605,
[90] Menegaldo LL, Fleury ADT, Weber HI (2003) Biomechanical modeling and optimal control of human posture. Journal of Biomechanics 36(11):1701–1712,
[91] Ong CF, Hicks JL, Delp SL (2016) Simulation-based design for wearable robotic systems: An optimization framework for enhancing a standing long jump. IEEE Transactions on Biomedical Engineering 63(5):894–903,
[92] Garcia-Vallejo D, Font-Llagunes JM, Schiehlen W (2016) Dynamical analysis and design of active orthoses for spinal cord injured subjects by aesthetic and energetic optimization. Nonlinear Dynamics 84(2):559–581,
[93] Felis M, Mombaur K (2013) Modeling and optimization of human walking. Cognitive Systems Monographs 18:31–42,
[94] Xiang Y, Arora JS, Abdel-Malek K (2011) Optimization-based prediction of asymmetric human gait. Journal of Biomechanics 44(4):683–693,
[95] Ong CF, Geijtenbeek T, Hicks JL, Delp SL (2019) Predicting gait adaptations due to ankle plantarflexor muscle weakness and contracture using physics-based musculoskeletal simulations. PLoS computational biology 15(10):e1006993,
[96] Meyer AJ, Eskinazi I, Jackson JN, Rao AV, Patten C, Fregly BJ (2016) Muscle synergies facilitate computational prediction of subject-specific walking motions. Frontiers in Bioengineering and Biotechnology 4(OCT),

[97] Halloran JP, Ackermann M, Erdemir A, van den Bogert AJ (2010) Concurrent musculoskeletal dynamics and finite element analysis predicts altered gait patterns to reduce foot tissue loading. Journal of Biomechanics 43(14):2810–2815,
[98] Ackermann M, van den Bogert AJ (2010) Optimality principles for model-based prediction of human gait. Journal of Biomechanics 43(6):1055–1060,
[99] Koelewijn AD, van den Bogert AJ (2016) Joint contact forces can be reduced by improving joint moment symmetry in below-knee amputee gait simulations. Gait and Posture 49:219–225,
[100] Verulkar A, Sandu C, Dopico D, Sandu A (2022) Computation of direct sensitivities of spatial multibody systems with joint friction. Journal of Computational and Nonlinear Dynamics 17(7),
[101] Maw N, Barber JR, Fawcett JN (1976) The oblique impact of elastic spheres. Wear 38(1):101–114,
[102] Banerjee JM, McPhee J (2013) Symbolic sensitivity analysis of multibody systems. Computational Methods in Applied Sciences 28:123–146,
[103] Shah H, Tripathi S, Lee LF, Krovi V (2010) Role of automated symbolic generation of equations of motion in mechanism and robotics education. In: Proceedings of the ASME Design Engineering Technical Conference, ASME, Montreal, Quebec, Canada, vol 2, pp 995–1002,
[104] Robertson DGE, Caldwell GE, Hamill J, Kamen G, Whittlesey SN (2014) Research Methods in Biomechanics, vol 73603966. Human Kinetics, Inc.,
[105] Ghannadi B, Mehrabi N, Razavian RS, McPhee J (2017) Nonlinear model predictive control of an upper extremity rehabilitation robot using a two-dimensional human-robot interaction model. In: Proceedings of the IEEE International Conference on Intelligent Robots and Systems, IEEE, Vancouver, BC, Canada, vol 2017-Septe, pp 502–507,
[106] Mehrabi N, Razavian RS, Ghannadi B, McPhee J (2017) Predictive simulation of reaching moving targets using nonlinear model predictive control. Frontiers in Computational Neuroscience 10:143,
[107] Carpenter MB (1968) The co-ordination and regulation of movements. Journal of Neuropathology and Experimental Neurology 27(2):348,
[108] Alexander RM (1984) The gaits of bipedal and quadrupedal animals. The International Journal of Robotics Research 3(2):49–59,
[109] Mombaur KD, Clever D (2017) Inverse optimal control as a tool to understand human movement. In: Laumond JP, , Mansard N, , Lasserre JB (eds) Geometric and numerical foundations of movements, vol 117, Springer, pp 163–186,
[110] Nasr A, Arami A, McPhee J (2019) Optimal cost function for predicting upper-limb movement with external load. In: Proceedings of the 16th annual Ontario Biomechanics Conference, Alliston, ON, Canada, p 1
[111] Flash T, Hogan N (1985) The coordination of arm movements: An experimentally confirmed mathematical model. Journal of Neuroscience 5(7):1688–1703,
[112] Neptune RR, Hull ML (1998) Evaluation of performance criteria for simulation of submaximal steady-state cycling using a forward dynamic model. Journal of Biomechanical Engineering 120(3):334–341,
[113] Anderson FC, Pandy MG (2001) Static and dynamic optimization solutions for gait are practically equivalent. Journal of Biomechanics 34(2):153–161,
[114] Razavian RS, McPhee J (2015) Minimization of muscle fatigue as the criterion to solve muscle forces-sharing problem. In: Proceedings of the ASME Dynamic Systems and Control Conference, ASME, Columbus, Ohio, USA, vol 1, p V001T15A001,
[115] Reinkensmeyer DJ, Wynne JH, Harkema SJ (2002) A robotic tool for studying locomotor adaptation and rehabilitation. In: Proceedings of the Annual International Conference of the IEEE Engineering in Medicine and Biology, IEEE, Houston, TX, USA, vol 3, pp 2353–2354,
[116] Shadmehr R, Holcomb HH (1999) Inhibitory control of competing motor memories. Experimental Brain Research 126(2):235–251,
[117] Jiroumaru T, Kurihara T, Isaka T (2014) Measurement of muscle length-related electromyography activity of the hip flexor muscles to determine individual muscle contributions to the hip flexion torque. SpringerPlus 3(1),
[118] Waters RL, Perry J, McDaniels JM, House K (1974) The relative strength of the hamstrings during hip extension. Journal of Bone and Joint Surgery - Series A 56(8):1592–

1597,
[119] Welsh P, Howitt S, Howarth SJ (2020) The influence of hip joint angle on the ratio between adduction and abduction torque in experienced, recreational male ice hockey players. International Journal of Sports Physical Therapy 15(1):22–33,
[120] Cahalan TD, Johnson ME, Liu S, Chao EY (1989) Quantitative measurements of hip strength in different age groups. Clinical Orthopaedics and Related Research 246:136–145,
[121] Neumann DA, Soderberg GL, Cook TM (1988) Comparison of maximal isometric hip abductor muscle torques between hip sides. Physical Therapy 68(4):496–502,
[122] Gupta A, Fernihough B, Bailey G, Bombeck P, Clarke A, Hopper D (2004) An evaluation of differences in hip external rotation strength and range of motion between female dancers and non-dancers. British Journal of Sports Medicine 38(6):778–783,
[123] Knapik JJ, Wright JE, Mawdsley RH, Braun J (1983) Isometric, isotonic, and isokinetic torque variations in four muscle groups through a range of joint motion. Physical Therapy 63(6):938–947,
[124] Hasson CJ, Miller RH, Caldwell GE (2011) Contractile and elastic ankle joint muscular properties in young and older adults. PLoS ONE 6(1),
[125] Hussain SJ, Frey-Law L (2016) 3D strength surfaces for ankle plantar- and dorsi-flexion in healthy adults: An isometric and isokinetic dynamometry study. Journal of Foot and Ankle Research 9(1),
[126] Tankevicius G, Lankaite D, Krisciunas A (2013) Test-retest reliability of biodex system 4 pro for isometric ankle-eversion and -inversion measurement. Journal of Sport Rehabilitation 22(3):212–215,
[127] Rannama I, Bazanov B, Baskin K, Zilmer K, Roosalu M, Port K (2013) Isokinetic muscle strength and short term cycling power of road cyclists. Journal of Human Sport and Exercise 8(2 PROC):19–29,
[128] Meyer C, Corten K, Wesseling M, Peers K, Simon JP, Jonkers I, Desloovere K (2013) Test-retest reliability of innovated strength tests for hip muscles. PLoS ONE 8(11),
[129] Poulmedis P (1985) Isokinetic maximal torque power of Greek elite soccer players. Journal of Orthopaedic and Sports Physical Therapy 6(5):293–295,
[130] Danneskiold-Samsoe B, Bartels EM, Bulow PM, Lund H, Stockmarr A, Holm CC, Wätjen I, Appleyard M, Bliddal H, Danneskiold-Samsoe B, Bartels EM, Bülow PM, Lund H, Stockmarr A, Holm CC, Wätjen I, Appleyard M, Bliddal H (2009) Isokinetic and isometric muscle strength in a healthy population with special reference to age and gender. Acta Physiologica 197(SUPPL. 673):1–68,
[131] Gonosova Z, Linduska P, Bizovska L, Svoboda Z (2018) Reliability of ankle–foot complex isokinetic strength assessment using the isomed 2000 dynamometer. Medicina (Lithuania) 54(3),
[132] Armour T, Forwell L, Litchfield R, Kirkley A, Amendola N, Fowler PJ (2004) Isokinetic evaluation of internal/external tibial rotation strength after the use of hamstring tendons for anterior cruciate ligament reconstruction. American Journal of Sports Medicine 32(7):1639–1643,
[133] Viola RW, Sterett WI, Newfield D, Steadman JR, Torry MR (2000) Internal and external tibial rotation strength after anterior cruciate ligament reconstruction using ipsilateral semitendinosus and gracilis tendon autografts. American Journal of Sports Medicine 28(4):552–555,
[134] Torry MR, Decker MJ, Jockel JR, Viola R, Sterett WI, Steadman JR (2004) Comparison of tibial rotation strength in patients' status after anterior cruciate ligament reconstruction with hamstring versus patellar tendon autografts. Clinical Journal of Sport Medicine 14(6):325–331,
[135] Karatsolis K, Nikolopoulos CS, Papadopoulos ES, Vagenas G, Terzis E, Athanasopoulos S (2009) Eversion and inversion muscle group peak torque in hyperpronated and normal individuals. Foot 19(1):29–35,
[136] Leslie M, Zachazeweski J, Browne P (1990) Reliability of isokinetic torque values for ankle invertors and evertors. Journal of Orthopaedic and Sports Physical Therapy 11(12):612–616,
[137] Aydog E, Aydog ST, Cakci A, Doral MN (2004) Reliability of isokinetic ankle inversion- and eversion-strength measurement in neutral foot position, using the Biodex dynamometer. Knee Surgery, Sports Traumatology, Arthroscopy 12(5):478–481,

[138] Kaminski TW, Perrin DH, Gansneder BM (1999) Eversion strength analysis of uninjured and functionally unstable ankles. Journal of Athletic Training 34(3):239–245
[139] Garner BA, Pandy MG (2001) Musculoskeletal model of the upper limb based on the visible human male dataset. Computer Methods in Biomechanics and Biomedical Engineering 4(2):93–126,
[140] Engin AE, Kaleps I (1980) Active muscle torques about long-bone axes of major human joints. Aviation Space and Environmental Medicine 51(6):551–555
[141] Hughes RE, Johnson ME, O'Driscoll SW, An KN (1999) Age-related changes in normal isometric shoulder strength. American Journal of Sports Medicine 27(5):651–657,
[142] Lewis MG, Yeadon MR, King MA (2021) Are torque-driven simulation models of human movement limited by an assumption of monoarticularity? Applied Sciences 11(9):3852,
[143] Morrison TM, Pathmanathan P, Adwan M, Margerrison E (2018) Advancing regulatory science with computational modeling for medical devices at the FDA's office of science and engineering laboratories. Medicine 5(SEP):1–11,
[144] Zhu Y, Zhang G, Zhang C, Liu G, Zhao J (2015) Biomechanical modeling and load-carrying simulation of lower limb exoskeleton. Bio-Medical Materials and Engineering 26(s1):S729–S738,
[145] Nasr A, Inkol KA, Bell S, McPhee J (2021) InverseMuscleNET: Alternative machine learning solution to static optimization and inverse muscle modelling. Frontiers in Computational Neuroscience 15:759489,
[146] Bell S, McPhee J (2022) Muscle torque generator model for a two degree-of-freedom shoulder joint. PhD thesis, University of Waterloo, Waterloo, ON, Canada
[147] Nasr A, McPhee J (2022) Multibody constrained dynamic modelling of human-exoskeleton: Toward optimal design and control of an active-passive wearable robot. In: Proceedings of the 6th Joint International Conference on Multibody System Dynamics and the 10th Asian Conference on Multibody System Dynamics, Springer, New Dehli, India, p 189
[148] Madeti BK, Chalamalasetti SR, Bolla Pragada SKsr (2015) Biomechanics of knee joint — A review. Frontiers of Mechanical Engineering 10(2):176–186,